nature materials

Supplementary information https://doi.org/10.1038/s41563-026-02568-9

Tuning phonon transmission via single-atom substituents

Table of contents

Supplementary Notes 2

Supplementary Figures 21

Supplementary Fig. 1. Estimate of the temperature- and gap-dependent thermal conductance via near-field thermal radiation at sub-10 nm gap sizes using the Derjaguin approximation.
Supplementary Fig. 2. Scanning electron microscopy images of an Au tip attached to the scanning calorimetric probe.
Supplementary Fig. 3. Fabrication process for the calorimetric scanning probe (CSP).
Supplementary Fig. 4. Characterization of the electrical properties of the NbN_x thin film and the Pt line.
Supplementary Fig. 5. Measurement schemes for characterizing the thermal response and the thermal conductance of the calorimetric scanning probe (CSP).
Supplementary Fig. 6. Thermal characterization of the calorimetric scanning probe (CSP).
Supplementary Fig. 7. Estimated thermal conductance and stiffness of the calorimetric scanning probe (CSP) from COMSOL simulations.
Supplementary Fig. 8. Illustration of the circuit used to measure the electrical conductance of junctions.
Supplementary Fig. 9. Schematic description of the setup employed for measuring the thermal conductance of junctions.
Supplementary Fig. 10. 2D histogram of the electrical and thermal conductance of *p*BDA-F molecular junctions.
Supplementary Fig. 11. 2D histogram of the electrical and thermal conductance of *p*BDA-Cl molecular junctions.
Supplementary Fig. 12. 2D histogram of the electrical and thermal conductance of *p*BDA-Br molecular junctions.
Supplementary Fig. 13. 2D conductance-displacement histogram of *p*BDA molecular junctions.
Supplementary Fig. 14. 2D conductance-displacement histogram of *p*BDA-F molecular junctions.
Supplementary Fig. 15. 2D conductance-displacement histogram of *p*BDA-Cl molecular junctions.
Supplementary Fig. 16. 2D conductance-displacement histogram of *p*BDA-Br molecular junctions.
Supplementary Fig. 17. 2D conductance-displacement histogram of *p*BDA-I molecular junctions.
Supplementary Fig. 18. Comparison of traces with and without thermal background conductance.
Supplementary Fig. 19. Characteristics of traces with zero background thermal conductances.
Supplementary Fig. 20. Characteristics of traces that do not feature an abrupt change in electrical conductance during rupture.
Supplementary Fig. 21. Traces plotted using raw data without a moving average.
Supplementary Fig. 22. Comparison of thermal conductance traces obtained using the rupture point analysis with and without a moving average.
Supplementary Fig. 23. Characterization of the settling time in our thermal measurements.
Supplementary Fig. 24. Additional analysis to support the robustness of the conclusions drawn from Fig. 4b.
Supplementary Fig. 25. Analysis of experimental uncertainty in the thermal conductance of single molecule junctions.
Supplementary Fig. 26. Junction geometries and stretching procedure.
Supplementary Fig. 27. Displacement-dependent thermal conductance.
Supplementary Fig. 28. Phonon transmission maps.
Supplementary Fig. 29. Analysis of the cumulative thermal conductance.
Supplementary Fig. 30. Cumulative thermal conductance as function of energy and displacement.
Supplementary Fig. 31. Eigenchannel-resolved phonon transmission.
Supplementary Fig. 32. Overlap of TEs and vibrational eigenmodes.
Supplementary Fig. 33. Model for phonon interference in two dimensions.
Supplementary Fig. 34. Model for the interference between two nearly degenerate vibrational modes.
Supplementary Fig. 35. Summary of interference features for the junction geometries shown in Fig. 5.
Supplementary Fig. 36. Analysis of phonon interference for the *p*BDA MJ around 3.2 meV.
Supplementary Fig. 37. Analysis of phonon interference for the *p*BDA-Br MJ at 6.4 meV.

Supplementary Tables 58

Table 1. Overview of the thermal conductance results shown in Supplementary Fig. 24b.
Table 2. Overview of the thermal conductance results for the studied molecular junctions.

Supplementary References 60

Experimental Approach

S1. Sample preparation and cleaning protocol

Preparation of substrate coated with molecules

In order to form a molecular layer on a clean gold (Au) surface, we started with a tantalum (Ta) substrate cleaned with isopropanol (IPA) and ultrasonication. Next, a 200 nm thick Au film was e-beam evaporated onto the Ta substrate using an Enerjet evaporator. After the deposition, this Au-coated substrate was baked at ~400 ºC at a vacuum of ~10^{-8} mbar in the preparation chamber of an ultra-high vacuum cryogenic scanning probe microscopy system (called CryoSPM in this work, Createc LT-STM/AFM). Subsequently, the Au surface on the substrate was cleaned with three cycles of oxygen (O_2) plasma using a PE-50-HF (Plasma Etch, Inc.). In each cycle, the oxygen plasma ran for 80 s with an RF power of 70 W. To create a layer of the studied molecules (*p*BDA and its derivatives, see Fig. 1c) onto the Au surface, we dissolved each of the studied molecules in ethanol (200 proof, anhydrous, ≥99.5%) and prepared a dilute molecular solution with a concentration of ~1-10 μmol/L in a glove box filled with ultra-high-purity (UHP) nitrogen (N_2). Then, a droplet of the prepared solution (~10 μL) was placed onto the fresh, clean Au surface. The Au surface with the molecular layer was subsequently rinsed with ethanol and dried in a stream of UHP N_2. Finally, the rinsed and dried substrate was immediately (within a few seconds of drying) transferred to the CryoSPM chamber, which was maintained at a vacuum of ~10^{-12} mbar. We note that all utensils used for preparing the molecular solutions were thoroughly cleaned with acetone and IPA, then dried with UHP N_2. We also note that 1,4-benzenedithiol (*p*BDA), with a purity of ≥99%, was purchased from Sigma-Aldrich. All derivatives of *p*BDA (see Fig. 1c), with a purity of ≥95%, were purchased from Sigma-Aldrich. All chemicals were used as received.

Preparation of the tip

The single Au crystal tip attached to the distal end of the custom-fabricated calorimetric scanning probe (CSP, see details of fabrication in section 2) was sharpened (to achieve a ~10 nm radius, see Fig. 1c and Supplementary Fig. 1a for examples) and cleaned using a scanning electron microscopy/focused ion beam (SEM/FIB) instrument (Helios 650), after which the probe was stored in a mild vacuum environment and quickly transferred into our UHV-STM instrument. We note that the probe cleaning approach is different from the substrate cleaning approach as the probe is easily damaged by the cleaning procedure employed for the substrate.

Local in-situ cleaning of the tip and substrate

We locally cleaned the Au surface by gently poking the Au tip into the Au substrate during measurements, which is a well-established process for local surface cleaning in STM-based experiments[1-4]. After this local cleaning procedure, a very low thermal conductance background, i.e., within experimental uncertainty, was typically established at which point we began the single-molecule junction measurements. We also note that the low-temperature environment is very critical, as it not only suppresses near-field thermal radiation (see Supplementary Fig. 1b) but also reduces diffusion of molecules on the surface. In general, this very low thermal conductance background can be maintained for several hours to up to a few days while repeatedly breaking and forming single molecule junctions. The local cleaning procedure was performed from time to time whenever a measurable thermal conductance background appeared. The procedure inevitably led to gradual blunting of the tip (see Supplementary Fig. 2 for an example) after several local cleaning operations. After that, a low thermal conductance background can no longer be achieved using the same tip and the probe was taken out of the STM and resharpened using a FIB. As a result, the measurements on each molecule were conducted using at least three different probe tips and Au-coated substrates with molecules (the substrate was also replaced when we took out the probe for replacement to ensure that the substrate was not contaminated during the probe exchange process). All probes and substrates were prepared strictly following the above cleaning procedures. Finally, we note that it takes more than a month to complete the measurement for each type of molecule.

Estimate of near-field thermal radiation at sub-10 nm gap sizes

We show in Supplementary Fig. 1b our calculation of the temperature- and gap-dependent near-field thermal conductance between an Au substrate and an Au tip for three different tip radii. These results, consistent with previous studies[5,6], were computed using the theory of fluctuational electrodynamics[7] and by employing the Derjaguin approximation[8], which is found to give excellent agreement with numerically exact techniques. The computational results indicate that for a 10-nm-radius Au tip (such as the one used in our experiments), the near-field thermal conductance between the Au tip and the Au substrate at 77 K is ~0.3 pW/K (for a gap size of 0.1–1 nm), a value smaller than the noise floor of our measurements. In contrast, if a larger radius tip (~400 nm) is used at room temperature, then the background thermal conductance is expected to be ~100 pW/K, a value significantly larger than the thermal conductance of a single molecule junction. Therefore, it is critical to probe thermal transport in single molecule junctions using a nanometrically sharp tip at cryogenic temperatures for greatly suppressing near-field radiative heat transfer between the tip and substrate.

We note that following the protocol described above enabled us to achieve negligible background conductance (i.e., the background thermal conductance is smaller than the uncertainty of our measurement scheme) on all the samples that we prepared. To substantially reduce surface contamination, both the tip and the substrate used for measurements must be cleaned thoroughly.

S2. Fabrication of CSPs

The steps involved in fabricating the CSPs employed in this work are shown in Supplementary Fig. 3a. We began with a bare Si wafer (500 µm thick). First (step 1), T-beams were defined onto the Si wafer using a deep reactive ion etching (DRIE) method, followed by a low-pressure chemical vapor deposition (LPCVD) of 600 nm of low-stress silicon nitride. After the growth of silicon nitride, a 30 nm thick serpentine platinum (Pt) line (step 2), with a 3 nm thick chromium (Cr) adhesive layer, was patterned via e-beam evaporation to form the Pt heater, as shown in Fig. 1b. Then (step 3), a 70 nm thick Au line, with a 5 nm thick Cr adhesive layer, was e-beam evaporated to build electrical connections to the serpentine Pt line and niobium nitride (NbN_x) thin film, which was sputtered in the next step (step 4). The NbN_x thin film (100 nm thick) was deposited in a LAB18 (Kurt J. Lesker) system using a niobium target (99.95% purity, purchased from Kurt J. Lesker) with a gas mixture of argon and nitrogen (Ar/N_2 = ~10 sccm : 6.7 sccm). In step 5, Au electrodes (500 nm thick) were patterned for wire bonding via e-beam evaporation. Subsequently (step 6), the suspended structure was created and released via backside etching using a reactive ion etching (RIE) for the silicon nitride and a DRIE for the silicon. After releasing the suspended structure (see Supplementary Fig. 3b), the probe was thoroughly cleaned in a Piranha solution and transferred to a Helios 650 for single Au crystal wire attachment (step 7), with the help of an integrated micromanipulator (omniprobe). Approximately 200 nm thick Pt was deposited at the interface of the attached Au wire and the Au surface of the probe to create a good electrical and thermal connection between the Au surface and the Au wire. In the final step (step

8), the attached Au wire was further sharpened using a focused ion beam to achieve a tip radius of ~10 nm. Supplementary Fig. 3c shows a CSP with an attached sharpened Au wire after step 8. The attached Au wire (99.99% purity, 5 μm diameter gold microwire) was purchased from Goodfellow.

S3. Characterization of CSPs

The heat current (Q) through a molecular junction (MJ), was quantified using $Q = G_{\mathrm{probe}}\times(T_{\mathrm{p}}–T_0)$, where T_{p} is the temperature measured by the $\mathrm{NbN_x}$ thermometer integrated into the probe and T_{o} is the ambient temperature and G_{probe} is the thermal conductance of the CSP. In order to employ the above equation, it is necessary to first characterize the temperature coefficient of resistance (TCR) of the thermometer and G_{probe}.

Characterization of the temperature coefficient of resistance (TCR) of the $\mathrm{NbN_x}$ thermometer and Pt heater

Our custom-fabricated CSP was installed into our CryoSPM system. The system was maintained at a vacuum of $\sim10^{-12}$ mbar and thermally stabilized at 77 K using liquid nitrogen. Then, the resistance of the integrated Pt line and the $\mathrm{NbN_x}$ thin film was measured using a four-probe method. To elaborate, a 1 μA AC current at 71 Hz was applied to the Pt line or the $\mathrm{NbN_x}$ thin film using a current source (Keithley 6221). The differential voltage across the Pt line or the $\mathrm{NbN_x}$ thin film was then measured using a lock-in amplifier (SR830, SRS). Next, the resistance of the Pt line and the $\mathrm{NbN_x}$ thin film was quantified as $R = \sqrt{2}\times V/I$, where the factor of $\sqrt{2}$ originates from the fact that the lock-in amplifier reads the root-mean-square (RMS) voltage. To characterize the TCR of the Pt line and the $\mathrm{NbN_x}$ thin film, the temperature of the CryoSPM system was varied and the resistances were measured as a function of temperature. Results from the measurements for the Pt line and the $\mathrm{NbN_x}$ thin film are shown in Supplementary Fig. 4a. As can be seen, in contrast to the widely used Pt serpentine lines, the $\mathrm{NbN_x}$ thin film exhibited a non-linear resistance change with respect to temperature, displaying the typical temperature-dependent behavior of a Mott insulator[9,10]. Hence, we fitted the resistance change in the $\mathrm{NbN_x}$ thin film with the function $R(T) = R_0\times\exp(T_0/T)^{1/4}$, where R_0 and T_0 are the fitting parameters in this Mott's variable range hopping model and T is the temperature at which the resistance was measured[9]. In our model, R_0 was determined to be 9.15 Ω and T_0, was 1.39×10^5 K. We used the fitted function to obtain the corresponding temperature coefficient of resistance ($\mathrm{TCR} = R^{-1}\times(\mathrm{d}T/\mathrm{d}R)$) of the $\mathrm{NbN_x}$ as a function of temperature. Similarly, we fitted the measured temperature-dependent resistance of the Pt line with a linear curve and extracted the TCR of the integrated Pt line accordingly. The obtained TCR corresponding to the resistance data in Supplementary Fig. 4a is presented in Supplementary Fig. 4b. As seen, the integrated $\mathrm{NbN_x}$ thin film had a much higher TCR (in terms of the absolute value) of ~ –2 %/K at 77 K and ~ –0.4 %/K at 290 K, respectively, compared to the integrated serpentine Pt line, which showed a TCR of ~0.3 %/K and ~0.19 %/K at 77 K and 290 K, respectively.

Characterization of the frequency response of the probe

We characterized the thermal response of the CSP by providing an AC current at a frequency f to the Pt heater to modulate the temperature of the probe at $2f$ (i.e., heating frequency f_{h}) due to Joule heating. We measured the AC temperature modulation of the CSP as a function of heating frequency by systematically varying the excitation frequency of the AC current (holding the amplitude of the current constant) and monitoring the voltage modulation at $2f$ ($\Delta V(2f)$) using the $\mathrm{NbN_x}$ thermometer. To elaborate, a 20 μA amplitude AC current at a frequency (f) was applied to the Pt line heater and a 15 μA DC current ($I_{\mathrm{NbNx,DC}}$) was applied to the $\mathrm{NbN_x}$ thermometer (its resistance is defined as R_{NbNx}) that was connected in series with a 10 kΩ potentiometer (see

Supplementary Fig. 5a). By varying the frequency of the applied AC current to the Pt line heater, the resulting temperature change of the CSP at $2f$ was obtained from:

$$\Delta T\left(2f\right)=\frac{\sqrt{2}\times\Delta V\left(2f\right)}{\alpha_{\mathrm{NbN_x}} I_{\mathrm{NbN_x,DC}} R_{\mathrm{NbN_x}}}, \tag{1}$$

We show in Supplementary Fig. 6a the results of the measured temperature change in the CSP as a function of heating frequency. As seen, the measured temperature change was frequency-independent below ~1 Hz and then decreased with the increasing heating frequency. The results show that the thermal cut-off frequency ($f_{\mathrm{c,thermal}}$), defined as the frequency at which the temperature response attenuates to its –3 dB value, was quantified to be ~11 Hz. This thermal cut-off frequency indicated the thermal response time of the CSP was approximately 15 ms, as estimated from $t_{\mathrm{thermal}} = 1/2\pi f_{\mathrm{c,thermal}}$.

Characterization of the thermal conductance of the probe

To characterize the thermal conductance of the probe we first supplied a DC current $I_{\mathrm{Pt,d.c.}}$ to the Pt heater and measured the temperature change of the probe via the $\mathrm{NbN_x}$ thermometer by supplying an AC current at frequency f to the $\mathrm{NbN_x}$ thermometer and measuring the voltage drop (($\Delta V(f)$) across the $\mathrm{NbN_x}$ thermometer at a frequency f, as illustrated in Supplementary Fig. 5b. The measured voltage drop was related to the temperature rise of the probe (ΔT) via the obtained R vs. T curve shown in Supplementary Fig. 4a. The data obtained from these experiments, when the supplied heat input (Q) was systematically varied, as $Q = I_{\mathrm{Pt,d.c.}}^2 R_{\mathrm{Pt}}$ is shown in Supplementary Fig. 4a (blue dots). Next, we also performed a second measurement where we supplied an AC current $I_{\mathrm{Pt,AC}}$ at a frequency ($f = 1$ Hz), at various amplitudes, to the Pt heater and measured the amplitude of temperature oscillations (ΔT) at $2f = 2$ Hz (a frequency well below the cutoff frequency identified in Supplementary Fig. 6a). Next, we measured the voltage drop across the $\mathrm{NbN_x}$ thermometer at $2f$ and related it to the amplitude of temperature modulation (see Supplementary Information for details). The measured data (ΔT vs. Q, quantified as $0.5\times I_{\mathrm{Pt,AC}}^2 R_{\mathrm{Pt}}$) from these experiments is shown in Supplementary Fig. 6b (yellow dots). As can be seen the measured data using these two techniques overlap when the applied power is identical and fall on a linear curve. The thermal conductance of the probe was directly obtained from the slope of the dashed linear line that is fit to the data ($G_{\mathrm{probe}} = Q/\Delta T = 1.1$ μW/K).

Finite element modeling of the thermal conductance of the probe

We further confirmed that the measured values of the thermal conductance were consistent with theoretical expectations by performing finite element modelling (FEM) using COMSOL. As shown in Supplementary Fig. 7a, we set a constant temperature of 77 K as a boundary condition to the end of the beams of the CSP. A 10 μW heat input was applied to the tip of the CSP and all remaining surfaces were treated as thermally insulated. The temperature distribution obtained from FEM is shown in Supplementary Fig. 7a. From a knowledge of the applied heat flux and the calculated temperature rise we estimated the thermal conductance of the probe to be ~1.2 μW/K, which closely agrees with our experimentally determined thermal conductance.

Finite element modelling of the stiffness of the probe

We note that the stiffness of the probe plays a critical role in performing thermal transport measurements in single molecule junctions. Therefore, we designed the CSPs with the geometry shown in Supplementary Figs. 7a and 3b, and Fig. 1b to have relatively high stiffness along the x,

y, z directions. The stiffness was estimated based on FEM using COMSOL. In the simulation, the ends of the beams were rigidly fixed. A 100 nN force was then applied to the tip of the CSP along the x, y or z directions and the deflections of the CSP along the respective directions were computed. The results of the displacement along the x, y and z directions are shown in Supplementary Figs. 7b–d. From these calculated displacements we estimated the stiffness of the probe to be approximately 4200, 1140, 17.3 N/m along the x, y, z directions, respectively. This stiffness is critical for creating stable molecular junctions that made it possible to perform minute-long measurements of thermal transport in single molecule junctions (see Fig. 2b and Supplementary Figs. 18–20). We note that the thermal conductivity, Young's modulus and Poisson's ratio of the silicon nitride used for the COMSOL calculations were 1.8 W/mK, 270 GPa and 0.27, respectively[11,12].

S4. Experimental approach for measuring the electrical and thermal conductance of molecular junctions

In order to successfully trap a single molecule junction, we adopted the well-established scanning tunneling microscopy break-junction (STMBJ) method[13]. Using this method, single molecule junctions can be formed between two Au electrodes by making mechanical contact between the Au tip of the CSP and the Au electrode coated with the desired molecules and separating them apart in a periodic fashion. In this process we first make a Au-Au contact and as the electrodes are separated we stochastically trap a single molecule junction between electrodes. To simultaneously measure the transient changes in both electrical and thermal conductance during the evolution of the junction, we employed the custom-fabricated CSP shown in Fig. 1b and Supplementary Fig. 3. The integrated gold (Au) line, serpentine platinum (Pt) line and niobium nitride (NbN_x) thin film served as the top tunneling electrode, heater and thermometer, respectively. Below, we elaborate on the experimental approach.

Measurement of the electrical conductance of atomic and molecular junctions

As seen in Fig. 1b and Supplementary Fig. 8, a high-frequency (1001 Hz) sinusoidal voltage (V_{bias}), sourced from a wavefunction generator (Hewlett Packard 33120A) with a voltage divider (1/10 V/V), was applied to the bottom Au surface. During the experiments, when a junction was formed between the two Au electrodes, which was connected in series with a fixed resistor ($R_{\mathrm{e},0}$, 100 kΩ), a non-negligible electrical current (I_{e}) started to flow in the circuit, as shown in Supplementary Fig. 8. To measure the electrical current (I_{e}) passing through the junction, a current-to-voltage amplifier (DLPCA200) was used to convert the current into a voltage signal (V_{e}). The voltage signal was then measured via a lock-in amplifier (SR830, SRS) with a time constant of 10 ms, which corresponds to an equivalent bandwidth of approximately 15.6 Hz. The electrical current (I_{e}) was then quantified as follows:

$$I_{\mathrm{e}} = \frac{\sqrt{2} g_{A/V} V_{\mathrm{e}}}{g_{V/V}} \quad . \tag{2}$$

Where $g_{A/V}$ and $g_{V/V}$ were the gains used for the current-to-voltage amplifier and the lock-in amplifier, respectively. In our measurements, $g_{A/V}$ and $g_{V/V}$ were set as 10^{-7} A/V and 1 V/V, respectively. As a result, the electrical conductance of the junction (G_{e}) can be calculated as follows:

$$G_{\mathrm{e}} = \frac{1}{R_{\mathrm{e}}} = \left(\frac{V_{\mathrm{bias}}}{I_{\mathrm{e}}} - R_{\mathrm{e},0} \right)^{-1} \quad . \tag{3}$$

We note that here the amplitude of V_{bias} was chosen to be 5 mV to ensure that the Joule heat generated by the electrical current (I_{e}) was negligible in the thermal measurements for both Au junctions and molecular junctions. With the help of the fixed resistor connected in series with the formed junction (see Supplementary Fig. 8), the measured range for the electrical conductance of junctions was extended and the effect of Joule heat was further diminished. To elaborate, the Joule heat dissipated within the junction can be quantified as follows:

$$Q = \frac{1}{2} R_{\mathrm{e}} I_{\mathrm{e}}^2 = \frac{1}{2} R_{\mathrm{e}} \left(\frac{V_{\mathrm{bias}}}{R_{\mathrm{e},0} + R_{\mathrm{e}}} \right)^2 \quad . \tag{4}$$

As indicated by Eq. (4), when a relatively small voltage bias was applied across the Au junctions or the molecular junctions, nearly half of the Joule heat was dissipated into each of the two electrodes[14], meaning half of the Joule heat was dissipated into the CSP. As a result, when a single Au atomic junction with an electrical conductance of $5G_0$ ($G_0 \approx 77.6$ μS) and a single molecular junction with an electrical conductance of $10^{-3}G_0$ were formed, the Joule heat dissipated in the CSP was approximately 6 pW and 0.5 pW, respectively. Considering that the applied temperature bias between the CSP and the bottom Au surface was ~30 K, the impact of Joule heating on the measured thermal conductance of the Au and molecular junctions was approximately 0.2 pW/K and 0.02 pW/K, respectively. These values were less than 1% of the measured thermal conductance of the Au junctions (~170 pW/K) and molecular junctions (~10 - 20 pW/K).

Measurement of the thermal conductance of atomic and molecular junctions

To measure the thermal conductance of the junctions, a DC current ($I_{\mathrm{Pt,d.c.}}$ = ~110 μA) was applied to the integrated Pt line to heat up the CSP by ~30 K (i.e., T_{P} = ~107 K), as shown in Supplementary Fig. 9. During the measurements, when a junction was formed between the two Au electrodes, the thermal pathway created by the junctions resulted in an additional temperature change ($\Delta T_{\mathrm{P}}(\mathrm{DC})$) of the CSP on the order of millikelvin (mK). This temperature change in the CSP induced a resistance change in the $\mathrm{NbN_x}$ thermometer ($R_{\mathrm{NbNx}}(\Delta T_{\mathrm{P}})$), which was measured using a half- bridge (see Supplementary Fig. 9). To quantify the resistance change in the $\mathrm{NbN_x}$ thermometer, a sinusoidal current ($I_{\mathrm{NbNx}}(\omega, \omega=2\pi f)$) at 71 Hz and 15 μA was applied to the half-Wheatstone bridge. The output of the bridge (ΔV_{J}) was first low-pass filtered using a voltage amplifier (SR560, SRS; the cut-off frequency was chosen to be 300 Hz) and then measured by a lock-in amplifier (SR830, SRS) with a time constant of 30 ms, corresponding to an equivalent bandwidth of ~5.2 Hz. As a result, the temperature change resulting from the formation, configuration change and rupture of the junctions can be obtained as follows:

$$\Delta T_{\mathrm{P}}(\mathrm{DC}) = \frac{\sqrt{2}\Delta V_{\mathrm{NbN_x}}(\omega)}{g_1 g_2 \alpha_{\mathrm{NbN_x}} R_{\mathrm{NbN_x}} I_{\mathrm{NbN_x}}} \quad . \tag{5}$$

Where g_1 (10 V/V), g_2 (10 V/V) were the gains used for the first-stage amplifiers and the second-stage amplifier, respectively. α_{NbNx} and R_{NbNx} were the TCR and resistance of the $\mathrm{NbN_x}$ thin film at ~107 K. $\Delta V_{\mathrm{NbNx}}(\omega)$ was the 1ω component of the voltage output. When a junction is formed, the small temperature change of the SCP also causes a resistance change in the platinum line, which leads to a small change in the heat dissipation in the SCP. Accounting for this effect, the thermal conductance of the junction (G_{th}) is given by:

$$G_{\mathrm{th}} = \frac{1}{R_{\mathrm{th,j}}} = \frac{\Delta T_{\mathrm{p}}\left(1-\alpha_{\mathrm{Pt}}\left(T_{\mathrm{p}}-T_{0}\right)\right)}{R_{\mathrm{th,probe}}\left(T_{\mathrm{p}}-T_{0}\right)} \quad . \tag{6}$$

Where T_0 is the environmental temperature (77 K), α_{Pt} is the TCR of the platinum line and $R_{\mathrm{th,probe}}$ is the thermal resistance of the CSP, i.e., the reciprocal of the measured thermal conductance of the probe (G_{probe}). We note that the amplitude and frequency of the sensing current (I_{NbNx}) were carefully chosen to obtain a good signal-to-noise ratio for thermal measurements and to avoid non-negligible Joule heat and displacement modulation between the two electrodes due to the modulated thermal expansion. We also note that the change in the heat dissipation of the resistive heater results in a systematic error ($\alpha_{\mathrm{Pt}}(T_{\mathrm{p}}-T_0) \sim 6\%$), which is relatively small and is corrected using Eq. (6) in our measurements. However, this systematic error can become significant if the selected resistive heater features a high TCR value or if the temperature bias used in the measurements is very large.

To enable thermal measurements of single molecule junctions that last up to a minute, we used a much slower pulling rate compared to the relatively fast speed (on the order of nm/s) used in most past studies on electrical measurements[15-17]. Specifically, a pulling rate of ~20 pm/s was used for Au atomic junctions, while a slower pulling rate of ~3-4 pm/s was employed when molecular junctions were present after the Au junctions ruptured. We note that in our measurements the Au tip was continuously displaced away from the Au surface and the junctions were gradually stretched until they ruptured.

S5. Overview of results for all studied molecular junctions

The 2D histograms for the electrical and thermal conductance of all MJs (*p*BDA-F, *p*BDA-Cl, *p*BDA-Br), that were not presented in the manuscript are shown in Supplementary Figs. 10–12. The histograms for *p*BDA-F, *p*BDA-Cl, *p*BDA-Br constructed from traces of MJs that are free of background conductance (see sections S6 and Methods) are shown in Supplementary Figs. 10, 11 and 12, respectively. As discussed in the main manuscript, the 1D histograms for electrical or thermal conductance were fitted with a Gaussian distribution, such a fitting procedure was widely used in past studies of electrical conductance of MJs[16-18]. The peak of the Gaussian fits represents the most probable electrical or thermal conductance of the MJs.

The averaged curves shown in Fig. 4a were obtained by performing an average as $G_c(t) = \frac{1}{N}\sum_{n=1}^{N} G_{c,n}\left(t-t_{r,n}\right)$ using junction traces that exhibited a sharp change in electrical conductance when the molecular junction ruptured (see Supplementary Figs. 18a–b and 19b–d). Here, $G_{c,n}(t-t_{r,n})$ represents the measured electrical conductance (G_{e}) or thermal conductance (G_{th}) of the n^{th} trace over time (t) and $t_{r,n}$ indicates the time at which the MJ ruptures in trace indexed by n, and N is the total number of traces used in the averaging method. A detailed description of how the signal to noise ratio is enhanced by this averaging method was described in previous work[14].

Additionally, we show in Supplementary Figs. 13–17 2D histograms of electrical conductance as a function of junction displacement for *p*BDA and *p*BDA derivatives. These 2D displacement histograms were created by aligning all junction traces to the rupture point of single Au atomic junctions.

For measuring the thermal conductance of each molecule, we collected approximately 1500 traces in total using at least three different samples coated with a molecular layer and three different tips attached onto the CSPs.

S6. Background conductance in thermal measurements

In this work, we developed an approach to effectively attenuate the background thermal conductance (i.e. the measured thermal conductance after the molecular junction is broken) to negligible levels (< 1 pW/K). This effectively zero background conductance (much smaller than the thermal conductance of a single molecule junctions) was achieved by gently poking the CSP onto the bottom Au surface to create a pristine junction with negligible background. Below we highlight the importance of eliminating this background conductance for performing thermal measurements on the atomic and molecular junctions.

To illustrate the impact of background thermal conductance on single molecule measurements, which was observed in all past work[19-22], we provide data in Supplementary Fig. 18c-d where we purposefully performed measurements in a situation where the background conductance was not eliminated (i.e., we chose not to follow our established protocol) and was ~few hundred pW/K – 1 nW/K (as is typical in past work[19-22]). In such a scenario, we find that the expected step-wise change in the thermal conductance of Au atomic junctions is smoothened out and the measured thermal conductance of the MJs shows a strong displacement (or time) dependence that is reflected in the conductance recording of a single trace (see Supplementary Fig. 18c-d or data (or extended data) provided in past work[19-22]). Further, after the MJ ruptured, the thermal conductance did not drop to the noise floor of the thermal signal, different from what was observed in clean junctions achieved in this work, as shown in Supplementary Fig. 18a-b. In strong contrast to the measured thermal conductance in a clean junction (Supplementary Fig. 18a-b) where the thermal conductance of a MJ shows a very weak dependence on tip displacement (few pW/K), the thermal conductance of junctions featuring a large background shows drifts that are almost an order of magnitude larger (~100s of pW/K) than the thermal conductance of a single molecule junction (~10 – 20 pW/K). These data highlight that achieving an effectively zero thermal background is critical for visualizing the impact of stretching on the thermal conductance of single molecule junctions and for precise measurements.

In our measurements, we employed the approach discussed above to reduce the thermal background to a negligible level (i.e., below the noise floor of the signal). When an effectively zero background was achieved, as seen in Supplementary Figs. 18, 19, 20 and Fig. 2b, the measured thermal conductance of the Au atomic junctions showed clear stepwise changes synchronized with the changes in the electrical conductance, and the measured thermal conductance of the molecular junctions was almost displacement-independent. When the molecular junction ruptured, as indicated an electrical conductance that is below the noise floor, the measured thermal conductance showed a concomitant but smaller change. Subsequently, a zero, flat, displacement-invariant thermal background was observed. Note that the slower response in the thermal signal is due to the applied moving average method, which is discussed in the next section.

S7. Application of moving average and analysis of the experimental uncertainty

To reduce the high-frequency noise in the measured thermal conductance signal, we employed a moving average on the raw data (~1000 points) of the thermal conductance signal. We show in Supplementary Fig. 21a–d plots of the raw data for four typical traces collected in our measurements, corresponding to Supplementary Figs. 19a and 18b–d. The data in Supplementary Figs. 21a and 19a correspond to Au junctions created on a clean Au surface (no molecules), while the data in Supplementary Figs. 21b and 19b corresponds to a *p*BDA-F junction with negligible background conductance. The data in the other two figure panels (Supplementary Figs. 21c, d and 18c, d) correspond to experiments with significant background conductance. We note that the moving average method, a standard signal process method known to have an effect similar to a low-pass filter, resulted in smoothening of rapid variations. Therefore, we optimized the moving average approach to ensure a good signal-to-noise ratio without completely smearing out the fine features of the step changes observed in the raw data of the measured thermal conductance. To confirm that the observed trends are not sensitive to the chosen averaging procedure, we show in Supplementary Fig. 22 the results obtained from the rupture point analysis for *p*-BDA and *p*-BDA-I single molecule junctions with the applied moving average method and without any moving average (same data as shown in Figs. 3a and 3b). We note that the observed "tail" in the traces shown in Figs. 3a-b and 4a for thermal conductance of single-molecule junctions is simply a reflection of the settling time associated with our thermal measurements as they involve, as part of the electronic measurement chain, a lock-in amplifier with a relatively long settling time. To prove this, we performed a control experiment (see Supplementary Fig. 23a), where we placed the probe far above the sample (i.e. the tip was not in contact with the sample). In this control experiment, we provided a small heat input to the probe by supplying a tiny current (I_{DC}, see Fig. Supplementary Fig. 23a), which was turned off at $t = 0$ s. This step change led to a small reduction in the temperature of the CSP, which was (for the purpose of this control) chosen to be very similar in magnitude to that expected when a single-molecule junction ruptures. The resulting temperature change in the measurement is shown in Supplementary Fig. 23a (without performing a moving average). From this measurement, it is clear that the time required to settle within 95% of the temperature change is ~0.65 s, which is consistent with the observed settling time for the measured thermal conductance in our measurements. To facilitate this comparison, we also show these results by overlaying them on our experimental data for the measurement of Au-*p*BDA-Au junctions in Supplementary Fig. 23b (without performing a moving average) and in Supplementary Fig. 23c (with a moving average). Note that the data for Au-*p*BDA-Au junctions are the same as those shown in Figs. 3a and 4a. As can be seen from the figures, the decay time and shape in the control experiment is ***almost identical*** to that observed in our molecular junction experiments, providing strong evidence that the observed "tail" is simply a reflection of the settling time of our measurement scheme.

To substantiate our findings from the rupture point analysis shown in Fig. 4, we performed additional analysis on the data shown in the top panel of Fig. 4a using different averaging ranges. Specifically, we computed the mean value and the standard deviation for each of the rupture point curves shown in the top panel of Fig. 4a by considering the data in five different intervals: [–20 pm, 0 pm], [–20 pm, –15 pm], [–15 pm, –10 pm], [–10 pm, –5 pm], [–5 pm, 0 pm]. The results from this analysis are shown in Supplementary Fig. 24a. It is evident from Supplementary Fig. 24a that in all these different averaging ranges the ordering of the thermal conductance of *p*BDA-derived junctions follows *p*BDA (or pBDA-F) > *p*BDA-Cl > *p*BDA-Br > *p*BDA-I, which is consistent with the expectation of a lower thermal conductance with increasing substituent mass. One can also see in Supplementary Fig. 24a that the thermal conductance of *p*BDA is not always higher than that of *p*BDA-F, especially for the displacement interval from –5 pm to 0 pm. We note that the flipping of order between the thermal conductances of the *p*BDA and *p*BDA-F junctions is also observed in the calculations shown in Supplementary Fig. 27. These results corroborate that due to the generally similar thermal conductance of *p*BDA and *p*BDA-F junctions, the ordering may be changed locally, but the global ordering (especially the strong suppression caused by Cl, Br and I) remains robust.

To further demonstrate the robustness of the relative order of thermal conductances, we present an alternative statistical study. We divide each of the five rupture point curves, shown in the top panel of Fig. 4a, into 1000 equally sized displacement intervals. For each interval, we determine the relative ordering of the thermal conductance and assign a value of 5 for the highest thermal conductance junction, 4 for the second highest thermal conductance junction, etc., down to 1 for the lowest thermal conductance junction. Subsequently we average the values of these assignments over all intervals for all the molecular junctions. The average weight orders obtained for Au-*p*BDA-Au, Au-*p*BDA-F-Au, Au-*p*BDA-Cl-Au, Au-*p*BDA-Br-Au, Au-*p*BDA-I-Au junctions are ~4.58, ~4.42, ~2.89, ~2.06, ~1.05, respectively. These results are shown in Supplementary Fig. 24b along with the data shown in Fig. 4b, as well as the average thermal conductance values from –20 pm to 0 pm and from –20 pm to –5 pm. It is obvious from Supplementary Fig. 24 that the thermal conductance ordering, as indicated by the data in Fig. 4b, is robust and representative in a global sense. We note that in Table 1 we present the exact values of the data shown in Supplementary Fig. 24b.

As discussed in the main manuscript and Methods, the 1D histograms of the measured electrical or thermal conductance were fitted with a Gaussian distribution. To quantify the experimental uncertainty for the measured conductances, we used varying amount of data (20%, 40%, 60%, 80% and 100%) to construct 1D histograms, which were then fitted with a Gaussian distribution. The mean value of the peaks of the Gaussian fits represented the thermal conductance and the standard deviation of the peaks indicated the experimental uncertainty of the thermal conductance (see Fig. 4b). Furthermore, we evenly divided the data into five sub-datasets and analyzed them using two different schemes (averaging scheme and histogram analysis). For each scheme, the mean value of the step change (averaging scheme for data shown in the top panel of Fig. 4a) or the mean of the fitted peak value (histogram analysis for data shown in the bottom panel of Fig. 4a) from the five sub-datasets represented the measured thermal conductance, and the standard deviation of the step changes or the peak values indicated the experimental uncertainty. More specifically, for the averaging scheme, we identified the thermal conductance at a representative displacement point (–15 pm) for each of the average curves obtained using the five sub-datasets and computed the mean value and standard deviation from the five data points. The results of these three uncertainty analyses for the thermal conductance of *p*BDA and its derivatives are compared in Supplementary Fig. 25. The same data obtained using the averaging scheme described above is also plotted in Fig. 4b. The findings show that the thermal conductances obtained from the three analyses are in good agreement. We also present in Table 2 the overview of results for the measured thermal conductance of all the molecular junctions studied in this work as obtained from the histogram analysis, with the uncertainty determined by the standard deviation of the fitted peak values with varying amount of data as described above.

Theoretical Modeling

S8. Selection of junction geometries and simulation of junction stretching

Note that experimental single-molecule transport studies, including this work, rely on conductance histograms obtained from a number of measurements that likely sample different electrode geometries. Hence, it is desirable to also conduct DFT calculations on a large ensemble of different junction geometries to compare the theoretical predictions with the experimental results. Unfortunately, due to the very large computational demand of the DFT calculations, such a comparison is not possible in this work. Therefore, we concentrated on the so-called top-top configuration, in which the explicitly included parts of the gold electrodes form atomically sharp pyramids (see the inset in Fig. 5a). We start with the initial top-top configuration to explore different junction configurations through junction compression and stretching. During the stretching process, the junctions undergo structural rearrangements, with the dominant reconfigurations occurring at the gold-anchor interface which covers part of the configurational space. In employing this approach, we assume that the trends of the thermal transport properties, for junctions made from the series of molecules (with single-atom substitutions) used in our study, are preserved and properly reflected by our DFT calculations. This assumption is convincingly supported by the remarkable consistency between our experimental measurements and DFT calculations. Therefore, the computational approach used in this work yields robust predictions of the thermal transport properties of the different molecular junctions.

For the simulation of the stretching of molecular junctions (MJs), the fixed parts of the electrodes are displaced along the transport direction in steps of 0.1 Å. At each step, the geometry is energetically optimized, and the transport properties are subsequently calculated. Near the rupture point, the displacement step size is decreased to 0.005 Å. The displacement-dependent total ground-state energy, as obtained from density functional theory (DFT), and the force, determined as the numerical derivative of energy vs. displacement, are shown as a function of electrode separation for all *p*BDA-derived MJs in Supplementary Fig. 26. In that figure, we also display the starting geometry for the *p*BDA MJ, which is a displacement-dependent minimum-energy configuration, and the geometry close to the rupture point. Note that we have set the zero of displacement to the displacement-dependent energetic minimum of each *p*BDA-derived MJ, such that an increase in the total energy is observed at negative displacements, if MJs are compressed (not shown in the plot). All junctions rupture at an applied force of 0.6 – 0.8 nN, close to the literature value for diamine anchors[23]. This rupture behavior is only obtained, if strict convergence criteria ("gcart 5") and the dispersion correction are applied.

We employ the so-called top–top configuration for all simulations, in which the explicitly included parts of the gold electrodes form sharp pyramids (see inset in Fig. 5a). This choice is motivated by technical considerations: in this geometry, the gold–anchor interface provides sufficient configurational freedom to relax properly, which is essential for reliable phonon calculations. Furthermore, this modeling yields stretching lengths comparable to the experimental traces. During the stretching process, the gold electrodes undergo structural rearrangements, with the dominant reconfigurations occurring at the gold–anchor interface.

High-resolution stretching traces with a displacement step of $\Delta d = 0.005$ Å close to rupture are considered for the phonon transport calculations, allowing for the sampling of a large configurational space rather than relying on a single junction snapshot.

By contrast, the commonly used hollow–hollow configuration[24] significantly reduces the achievable stretching lengths for relatively stiff molecules with weak diamine anchors, as considered in this work, and imposes strict geometric constraints during the construction of the junction[25].

The qualitative trends observed within the pBDA molecule set are robust even when using a highly minimalistic description of the electrodes based on a Debye model, as demonstrated in the recent publication[26] (see Fig. S1 in this reference). This indicates that the observed modulation originates from an internal molecular effect rather than from details of the electrode modeling.

S9. Phonon transport

Analysis of the thermal conductance

The calculated thermal conductances of all pBDA-derived MJs are shown in Supplementary Fig. 27. The conductances generally decrease with increasing displacement. The ordering within the family of pBDA derivatives is rather robust: The halogen substituents reduce the thermal conductance with increasing mass. For certain molecules the thermal conductance is quite similar in our calculations, namely pBDA and pBDA-F as well as pBDA-Br and pBDA-I. For the two pairs of molecules the order of the thermal conductance is inverted at particular electrode displacements.

The corresponding phonon transmissions as function of energy and displacement are shown in Supplementary Fig. 28 in the form of a two-dimensional contour plot. The transmission maps can be divided into a low-energy region up to approximately 7.5 meV and a high-energy region from 7.5 meV to 25 meV. As discussed in the main text, the transmission in the low-energy region decreases with increasing substituent mass, while the energetic position of transmission resonances is nearly unaffected by displacement. In the high energy range, the pBDAs exhibit two transmission peaks that start near 11 and 18 meV and are shifted to lower energies with increasing electrode separation. Overall, the transmission maps of the pBDA-derived MJs are quite similar, showing that the chosen molecules form a consistent set.

To analyze the displacement dependence of the cumulative thermal conductance, we apply the method explained in Supplementary Fig. 29. This figure shows the cumulative thermal conductance of the pBDA MJ in its minimum energy geometry in blue, along with the corresponding transmission in red. We use a threshold of 0.2 for the phonon transmission, as indicated by the horizontal line, to identify energy regions relevant for the thermal conductance. Whenever the transmission exceeds this threshold, we define this as the start of a relevant energy region, which ends when the transmission drops below the threshold again. An identified region starts at a solid green vertical line and extends to the following dashed green line. The difference in cumulative thermal conductance between the start and the end of each region is the contribution of the identified peak structure to the overall conductance. In regions outside of the identified peak features, a background conductance remains.

The cumulative thermal conductances as a function of energy and displacement for all pBDA-derived MJs, as determined with the described method, are shown in Supplementary Fig. 30. The analysis confirms that the reduction in thermal conductance for increasing mass of substituents, described in the main text, is indeed caused by the disappearance of constructive interferences in the low-energy region near 3.5 meV and that this feature remains stable across the entire displacement range (see the orange- or red-colored line for the pBDA junction and its analogs for the substituted pBDA MJs). In addition, the contribution of certain transmission peaks to the cumulative thermal conductance decreases for all pBDA derived MJs, particularly for $d > 1.5$ Å, which explains the general reduction of the thermal conductance as a function of displacement shown in Supplementary Fig. 27.

Decomposing phonon transmission eigenchannels into vibrational eigenmodes

The concept of transmission eigenchannels (TEs) is useful for understanding transport mechanisms in MJs. Initially developed for electronic transport[25,27], they have been used for distinguishing through-space and through-bond transport[28] or for studying the coupling of electronic states with π or σ symmetry in conjugated hydrocarbons[25]. Subsequently they have been extended to phonon transport[29].

In two-terminal devices, TEs consist of an incoming part of the wavefunction in one electrode, a backscattered part in the same electrode, the wavefunction in the scattering region of the central junction part, and the transmitted wavefunction in the other electrode. Similar to electronic TEs, phononic TEs allow to decompose the total transmission $\tau_{\mathrm{ph}}(E)$ into transmission probabilities $0 \leq \tau_{\mathrm{ph},\mu}(E) \leq 1$, obeying the relation $\tau_{\mathrm{ph}}(E) = \sum_{\mu} \tau_{\mathrm{ph},\mu}(E)$. Associated with the transmission probability $\tau_{\mathrm{ph},\mu}(E)$ is the wavefunction of the TE μ. Its projection on the central junction part can be determined from quantities that are accessible in a phonon transport code, as described in detail in Ref. [29]. The atomic displacements in the central junction region can be expressed as

$$\widetilde{\boldsymbol{Q}}_{\mu}(E) = \sum_{i \epsilon C, \alpha} \frac{s(E)}{\sqrt{m_i}} \left| a_{i\alpha,\mu}(E) \right| e^{i\theta_{i\alpha,\mu}(E)} \boldsymbol{e}_{i\alpha} \ . \tag{7}$$

Here, the $a_{i\alpha,\mu}(E)$ are complex expansion coefficients with phase $\theta_{\mu\alpha,i}(E)$, $s(E)$ is an energy-dependent scaling factor, m_i is the mass of the ith atom, and the $\boldsymbol{e}_{i\alpha}$ are unit vectors that describe the displacement of atom i into the Cartesian direction α. For visualization of phononic TEs, the real part of $\widetilde{\boldsymbol{Q}}_{\mu}(E)$ is typically plotted[29].

The decomposition of the total transmission into TE contributions needs to be computed independently at each energy E of the incoming wave. Typically, the TEs are sorted according to the magnitude of the transmission eigenvalues $\tau_{\mathrm{ph},\mu}(E)$ at each E, regardless of any crossings. Here we trace the TEs instead based on their wavefunctions and identify them with Greek letters (α, β, γ, …). The ordering of the TE labels is essentially arbitrary. For practical reasons, we assign the Greek letters in alphabetical order according to the size of the eigenvalues $\tau_{\mathrm{ph},\mu}(E)$ at E=18 meV. In principle, $3N$ eigenchannels exist, if the central region consists of N atoms. However, the number of TEs with a significant $\tau_{\mathrm{ph},\mu}(E)$ is limited by the narrowest part of the junction[30]. Since the amine anchors of the *p*BDA derivatives bind to the gold electrodes via single Au-N bonds, we expect a significant contribution $\tau_{\mathrm{ph},\mu}(E)$ only from up to three TEs, namely two TEs of basically transverse and one of longitudinal character[29].

Supplementary Fig. 31 shows the TE-resolved phonon transmission of the *p*BDA-derived MJs at the same displacement (d = 0.8 Å) as used in Fig. 5a of the main text. We indeed observe for all MJs that at most three TEs yield a significant contribution to the total transmission and hence we show only the transmissions of TEs α, β, γ. Multiple TEs furthermore contribute only up to energies of around 7.5 meV, whereas only one eigenchannel remains for all *p*BDA-derived MJs above this energy. It is also well visible in the plot that the contributions of TEs β, γ are reduced for larger substituent masses. In the case of the *p*BDA-I MJ, for example, the transmissions of β and γ TEs remain consistently below 10^{-1}.

As a new methodological development, we decompose here the TEs into the vibrational eigenmodes of the central system. To correlate the eigenenergies $\epsilon_i(E)$ of the vibrational modes with the energies of the peaks in the phonon transmission, we find it important to consider the embedding self-energies $\Pi^{\mathrm{r}}_X(E)$ of the electrodes $X = \mathrm{L}, \mathrm{R}$. Thus, the characteristic equation of the central system is given by

$$[K_{\mathrm{CC}} + \Pi^{\mathrm{r}}_{\mathrm{L}}(E) + \Pi^{\mathrm{r}}_{\mathrm{R}}(E)]\boldsymbol{u}_i(E) = \epsilon_i^2(E)\boldsymbol{u}_i(E) \quad . \tag{8}$$

We project the complex atomic displacements of the eigenchannel $\tilde{\boldsymbol{Q}}_\mu(E)$ onto the complex atomic displacements of the central system $\boldsymbol{u}_i(E)$ to determine the overlap

$$\sigma_{\mu i}(E) = \left|\tilde{\boldsymbol{Q}}_\mu(E)\boldsymbol{u}_i^*(E)\right| \tag{9}$$

between a TE μ and the vibrational eigenmode i of the central systems. The asterisk marks the complex conjugate. In this way, we can be resolve for each eigenchannel, which vibrational modes contribute most to transport at a particular energy E.

Supplementary Fig. 32 shows the overlap $\sigma_{\alpha i}(E)$ for all *p*BDA-derived MJs at the displacement $d = 0$ Å, i.e. the overlap of a vibrational eigenmode i with the TE α. The imaginary part of the vibrational eigenmode i is associated with an energetic broadening, which is indicated by the width of lines in the plots. In general, we find that the larger the energetic broadening is, the stronger is also the energy dependence of the eigenmodes ϵ_i due to the embedding self-energies. Furthermore, the plots show that transport for a given phonon energy is carried by eigenmodes, whose energies are close to that phonon energy, i.e. ϵ_i is typically similar to E. An analogy to electronic transport is that, for instance, if the HOMO level is close to the Fermi energy, transport is primarily carried by this orbital.

The asymmetry of vibrational modes, induced by the substituents, is evident here as well, as energetic degeneracies of the modes are lifted for heavier substituents. This can be seen, for example, in the range $5\ \mathrm{meV} < \epsilon_i < 10\ \mathrm{meV}$ for the *p*BDA MJ in Supplementary Fig. 32a as compared to the *p*BDA-I MJ in Supplementary Fig. 32e. Overall, the described analysis allows us to determine for each TE μ at energy E, which vibrational eigenmodes ϵ_i carry the transport.

S10. Quantum interferences in phonon transport

Quantum interference in electron transport through MJs can be understood by considering the symmetries of frontier orbitals of isolated molecules[31]. Orbital interference is studied in energy space, and frontier orbitals are usually plotted to analyze symmetries visually[32,33]. In phononic transport, the analogous entities to molecular orbitals are the vibrational eigenmodes of the open quantum system. We explain here, how the concept of orbital interference in electron transport can be generalized to phonon heat transport. Based on this, we also show how illustrations of eigenmodes should be interpreted to assess, if they interfere constructively or destructively.

Following ideas presented in Refs. [34,35], we work out the analysis here more systematically, starting from the formula for the phonon transmission. We assume that the left and right electrodes couple, as described by the linewidth broadening matrixes $\Lambda_X(E) = \mathrm{i}[\Pi^{\mathrm{r}}_X(E) - \Pi^{\mathrm{a}}_X(E)]$ (see the main text), in a similar fashion only to those atoms of the central region that are closest to the two

L-C and C-R interfaces, see Supplementary Fig. 26a. The phonon transmission can then be approximated to zeroth order by[34]

$$\tau_{\mathrm{ph}}(E) \propto \mathrm{Tr}\left[D_{\mathrm{lr}}^{(0),\mathrm{r}}(E) D_{\mathrm{rl}}^{(0),\mathrm{a}}(E)\right] = |P_{\mathrm{lr}}(E)|^2 \quad , \tag{10}$$

with $D_{\mathrm{rl}}^{(0),\mathrm{a}}(E) = \left[D_{\mathrm{lr}}^{(0),\mathrm{r}}(E)\right]^{\dagger}$ and the shortcut $|P_{\mathrm{lr}}(E)|^2$ for the trace of the squared propagator. In the expression, subscripts l and r denote terminal atoms on the left and right sides of the junction, respectively, together with their Cartesian components, while superscripts r and a stand for retarded and advanced. Due to the construction of our ECC in the ab-initio calculations, the terminal atoms are three gold atoms on both the left and right sides of the central region (see Supplementary Fig. 26a). The zeroth-order retarded Green's function $D_{\mathrm{lr}}^{(0),\mathrm{r}}(E)$ can be computed using the spectral representation

$$D_{\mathrm{lr}}^{(0),\mathrm{r}}(E) = \sum_{k} \frac{\boldsymbol{u}_k^{\mathrm{l}}(E_{\mathrm{d}})[\boldsymbol{u}_k^{\mathrm{r}}(E_{\mathrm{d}})]^{\dagger}}{(E+i\eta)^2 - \epsilon_k(E_{\mathrm{d}})^2} \quad . \tag{11}$$

The sum runs over all vibrational eigenmodes k of the central system, $\epsilon_k(E_{\mathrm{d}})$ are the energies of the eigenmodes, and the vectors $\boldsymbol{u}_k^{\mathrm{l}}(E_{\mathrm{d}})$ and $\boldsymbol{u}_k^{\mathrm{r}}(E_{\mathrm{d}})$ contain the coefficients of the eigenmodes of the terminal atoms in the l and r subspaces, respectively. The energies $\epsilon_k(E_{\mathrm{d}})$ and vectors $\boldsymbol{u}_k^{\mathrm{l}}(E_{\mathrm{d}})$, $\boldsymbol{u}_k^{\mathrm{r}}(E_{\mathrm{d}})$ are obtained from the diagonalization in Eq. (8) at the energy E_{d}. (For three gold atoms in the l and r subspaces, $D_{\mathrm{lr}}^{(0),\mathrm{r}}(E)$ is hence a 9×9 matrix due to the three Cartesian components in three-dimensional space.)

Due to the evaluation of the diagonalization at E_{d}, the analysis that is presented in the following is valid around this energy. Interference of vibrational eigenmodes can hence be studied locally in energy space using $|P_{\mathrm{lr}}(E)|^2$. The conditions for constructive and destructive interference will be derived in the next subsection using a simple model system, where only single atoms on left and right sides of the central part couple to left and right electrodes. This will be followed by an extension to coupling to two atoms on the left and right sides.

Model for coupling to single atoms in two dimensions

To develop a better understanding of phononic interference effects, we consider a simplified system. We study a MJ in two dimensions, where single atoms on the left and right sides of the central region are coupled to the electrodes. Thus $\boldsymbol{u}_k^{\mathrm{l}}(E_{\mathrm{d}}) = (x_k^{\mathrm{l}}, y_k^{\mathrm{l}})^T$ and $\boldsymbol{u}_k^{\mathrm{r}}(E_{\mathrm{d}}) = (x_k^{\mathrm{r}}, y_k^{\mathrm{r}})^T$ are the two-dimensional displacement vectors. We assume that the energy E_{d}, at which we want to analyze the interference, lies precisely in the middle of the energies of two eigenmodes $\epsilon_i < E_{\mathrm{d}} < \epsilon_{i+1}$, i.e. $E_{\mathrm{d}} = (\epsilon_i + \epsilon_{i+1})/2$. Due to the decreasing importance of distant modes, based on the energy dependence of the denominator in Eq. (11), we restrict our analysis to the two modes i and $i + 1$ in the summation of Eq. (11). The summands in Eq. (11) are then given by (terms are subtracted due to the different signs of the denominator)

$$|P_{\mathrm{lr}}(E_{\mathrm{d}})|^2 \propto [(x_i^{\mathrm{l}} x_i^{\mathrm{r}} - x_{i+1}^{\mathrm{l}} x_{i+1}^{\mathrm{r}})^2 + (y_i^{\mathrm{l}} y_i^{\mathrm{r}} - y_{i+1}^{\mathrm{l}} y_{i+1}^{\mathrm{r}})^2 + m] \tag{12}$$

with

$$m = (x_i^{\mathrm{l}} y_i^{\mathrm{r}} - x_{i+1}^{\mathrm{l}} y_{i+1}^{\mathrm{r}})^2 + (y_i^{\mathrm{l}} x_i^{\mathrm{r}} - y_{i+1}^{\mathrm{l}} x_{i+1}^{\mathrm{r}})^2 .$$

being terms that mix Cartesian components. These mixed terms are neglected for the classification of interference features.

The model calculation thus shows that $|P_{\mathrm{lr}}(E)|^2$ and hence the transmission $\tau_{\mathrm{ph}}(E)$ are determined by the Cartesian components of the eigenmodes at the anchoring atoms. Constructive interference between two modes occurs, if the products $x_i^{\mathrm{l}} x_i^{\mathrm{r}}$ and $x_{i+1}^{\mathrm{l}} x_{i+1}^{\mathrm{r}}$ have different signs and yield similar absolute values, as their contributions add up in this case. This happens for parallel motion in one eigenmode and anti-parallel motion in the other. Conversely, destructive interference arises, if the products $x_i^{\mathrm{l}} x_i^{\mathrm{r}}$ and $x_{i+1}^{\mathrm{l}} x_{i+1}^{\mathrm{r}}$ have the same sign and similar absolute value, leading to cancellation of contributions. This is fulfilled for either parallel or antiparallel mode displacements in both modes i and $i + 1$. Interferences can be weakened, if the products $x_i^{\mathrm{l}} x_i^{\mathrm{r}}$ and $x_{i+1}^{\mathrm{l}} x_{i+1}^{\mathrm{r}}$ differ in absolute values, as in this case for example contributions do not completely cancel out. In the extreme case that atoms in the l and r subspaces swing exclusively along x for mode i and along y for mode $i + 1$, the expressions show that no interference arises.

Model calculation for coupling to multiple atoms in two dimensions

In this section, we study the interference rules in the case, where multiple atoms are coupled to the left and right electrodes. We assume a point symmetry with respect to the atoms on left and right sides that are at the L-C and C-R interfaces, see Supplementary Fig. 33, similar to what is assumed in our three-dimensional ab-initio phonon transport calculations later on. For the sake of simplicity, we consider only the longitudinal transport component, making the model effectively one-dimensional. The vectors in the numerator of Eq. (11) are now defined by $\boldsymbol{u}_k^{\mathrm{l}}(E_{\mathrm{d}})=(x_{1,k}^{\mathrm{l}}, x_{2,k}^{\mathrm{l}})^T$ and $\boldsymbol{u}_k^{\mathrm{r}}(E_{\mathrm{d}})=(x_{1,k}^{\mathrm{r}}, x_{2,k}^{\mathrm{r}})^T$, where the subscripts 1 and 2 mark the atoms, see Supplementary Fig. 33. The results for $|P_{\mathrm{lr}}(E)|^2$ are identical to the previous section, if we identify $x_{1,k}^{\mathrm{l}} = \mathrm{x}_k^{\mathrm{l}}$, $x_{2,k}^{\mathrm{l}} = y_k^{\mathrm{l}}$, $x_{1,k}^{\mathrm{r}} = x_k^{\mathrm{r}}$, $x_{2,k}^{\mathrm{r}} = \mathrm{y}_k^{\mathrm{r}}$. The squared propagator and hence the transmission are thus primarily determined by products such as $\left(x_{1,i}^{\mathrm{l}} x_{1,i}^{\mathrm{r}} - x_{1,i+1}^{\mathrm{l}} x_{1,i+1}^{\mathrm{r}}\right)^2$ and similarly for atom 2. If we neglect again the mixed terms, summarized in m, the rules for interferences from the previous chapter can be directly applied.

The reasoning illustrates that the Cartesian components of the displacement vectors of the relevant atom pairs (1 on the left and 1 on the right etc.) must be compared. In general, the pairing of atoms in the l and r subspaces is determined by the geometry of the junction that is ultimately encoded in the linewidth broadening matrices.

Interference for nearly degenerate vibrational eigenmodes

In the previous description, a certain energetic splitting of the interfering vibrational modes i and $i + 1$ is always assumed. In phononic transport, a peculiar phenomenon arises when the eigenmodes are energetically nearly degenerate. More precisely, the energy splitting of the two vibrational modes needs to fall below the broadening of the transmission resonances that are related to the modes i and $i + 1$. A one-dimensional model for two constructively or destructively interfering vibrational eigenmodes is shown in Supplementary Fig. 34. As visible and discussed so far, for a sufficiently large energy splitting that is larger than the broadening of the eigenmode-related transmission resonances, an enhanced $|P_{\mathrm{lr}}(E)|^2$ is observed between these modes in the constructively interfering case and a suppression for the destructively interfering case. If the modes get nearly degenerate, however, the situation is reversed, and $|P_{\mathrm{lr}}(E)|^2$ of the constructively interfering case falls below those of the destructively interfering case. In this case, the transmission may be substantially smaller than 1 for the situation of constructive interference. These findings agree with a remark in Ref. [35], but are derived here systematically.

Summary of interference rules for vibrational eigenmodes

From the discussion above, we have identified sufficient conditions for vibrational modes to interfere constructively or destructively. Let us consider energies $\epsilon_i < E < \epsilon_{i+1}$ between two vibrational eigenmodes i and $i + 1$. For the two vibrational modes, we concentrate on the displacements of those atoms of the central region that are located at the interface to the left or right electrode. Based on the junction geometry, we identify relevant atom pairs on the left or right sides. (i) The interference between the modes i and $i + 1$ is constructive, if the motion of the atom pairs is antiparallel for one mode and parallel for the other, whereas (ii) the interference between the modes i and $i + 1$ is destructive, if the motion of the atom pairs of both modes is either parallel or antiparallel. In the case of constructive interference, there is a special case, where the transmission can still be low between the modes, if their energies are nearly degenerate. If the atomic displacements of the terminal atom pairs in both modes i and $i + 1$ do not point into the same direction or no consistent pairing of parallel or antiparallel motion of atoms can be found between the two modes, interference will typically be weak.

Resolving transmission eigenchannels in terms of vibrational eigenmodes in ab-initio calculations

With the explanations provided above for simple model systems, we now return to the full ab-initio results, where the transmission may be carried by different TEs (see Supplementary Fig. 31). To study, how the TEs can be resolved into vibrational eigenmodes, and to understand the interference properties of the vibrational modes, we introduce an index for the TE μ and redefine the propagator as

$$\tau_{\mathrm{ph},\mu}(E) \propto \mathrm{Tr}\left[D^{(0),\mathrm{r}}_{\mathrm{lr},\mu}(E) D^{(0),\mathrm{a}}_{\mathrm{lr},\mu}(E)\right] = \left|P^{\mu}_{\mathrm{lr}}(E)\right|^2 \tag{13}$$

with the zeroth-order retarded Green's function

$$D^{(0),\mathrm{r}}_{\mathrm{lr},\mu}(E) = \sum_{k,\sigma_{\mu k}>t} \frac{\boldsymbol{u}^{\mathrm{l}}_k(E_\mathrm{d})[\boldsymbol{u}^{\mathrm{r}}_k(E_\mathrm{d})]^\dagger}{(E+i\eta)^2 - \epsilon_k(E_\mathrm{d})^2}. \tag{14}$$

Here the sum is restricted to run only over eigenmodes k with an overlap $\sigma_{\mu k}$ to the TE μ that is larger than the threshold t. Throughout the work we use $t = 0.2$ as threshold. With this definition $\left|P^{\mu}_{\mathrm{lr}}(E)\right|^2$ correlates well with the phonon transmission $\tau_{\mathrm{ph},\mu}(E)$ of eigenchannel μ around the energy E_d, at which the characteristic Eq. (11) of the central systems was solved to determine the eigenenergies $\epsilon_k(E_\mathrm{d})$ and eigenvectors $\boldsymbol{u}^{\mathrm{l}}_k(E_\mathrm{d})$, $\boldsymbol{u}^{\mathrm{r}}_k(E_\mathrm{d})$. The propagator allows us to classify the interference effects, i.e. constructive, destructive or not present. We note that different TEs show distinct transmissions and interference characteristics, and it is hence important to distinguish them through the index μ.

The classification of phonon interferences in a TE μ can be carried out in two different ways: (i) mathematically through Eq. (14) and (ii) visually through illustrations of atomic displacements of the contributing modes. Both procedures are used in Fig. 5 of the main text.

Classification of vibrational interference for *p*BDA-derived molecular junctions

The interference of vibrational modes is classified in Supplementary Fig. 35 for all *p*BDA-derived MJs, based on the geometries shown in Fig. 5. In Supplementary Fig. 35, the same energy regions as in Fig. 5a are marked by the dashed vertical lines. Around 3.2 meV, the *p*BDA MJ exhibits constructive interferences in the β and γ TEs, while TE α does not contribute significantly to the total phononic transmission. With increasing substituent mass, the constructive interferences are progressively weakened. Specifically, for *p*BDA-Br and *p*BDA-I MJs, no constructive interference is observed in the β eigenchannel. Around 3.8 meV, the same pattern is found. *p*BDA, *p*BDA-F, and *p*BDA-Cl MJs exhibit constructive interferences, whereas these constructive interferences are significantly weakened by the substituent-induced asymmetry of vibrational modes for *p*BDA-Br and *p*BDA-I MJs. At 6.5 meV, some constructive interferences result in a less strongly enhanced transmission, especially for *p*BDA and *p*BDA-F MJs, due to energetically nearly degenerate interfering modes. For the *p*BDA-Cl MJ, a significant asymmetry of interfering vibrational modes is already evident, which decreases the transmission. For *p*BDA-Br and *p*BDA-I MJs, the constructive interferences are so strongly disrupted by the asymmetry that they are no longer visible. The *p*BDA-Br and *p*BDA-I MJs exhibit the antiresonances, described in the context of Fig. 5, at energies of around 19.0 and 16.8 meV.

Overall, it is evident that the decreasing thermal conductance within the family of *p*BDA-derived MJs results primarily from the weakening of constructive interferences in the low-energy ranges near 3.5 and 6.5 meV (see also the analysis of the cumulative thermal conductance in Supplementary Fig. 30). Destructive interferences contribute to a lesser extent to the observed differences between the *p*BDA-derived MJs. The transmission features at low energy are more important for the thermal conductance due to the weighting function $W_{\mathrm{ph}}(E,T)$ (see Eqs. (5) and (6) of the main text). Because of the characteristics of the Bose-Einstein distribution, $W_{\mathrm{ph}}(E,T)$ considers increasingly the low energy regions of the transmission for decreasing temperature.

The interference features in Supplementary Fig. 35 were classified using the rules derived in previous sections. To demonstrate the corresponding analysis, we will present three examples in the following.

Vibrational interference in the TEs β and γ is analyzed for the *p*BDA MJ around 3.2 meV in Supplementary Fig. 36. It is evident that the energies of the vibrational eigenmodes coincide with the peak positions of the transmission in the corresponding TEs. The propagators $|P^{\beta}_{\mathrm{lr}}(E)|^2$ and $|P^{\gamma}_{\mathrm{lr}}(E)|^2$ show a similar behavior with maxima at the eigenmodes. The identified constructive interferences are apparent from the rules presented in the previous sections. In particular, the eigenmode 1 shows a parallel motion of the indicated atom pairs, whereas they move antiparallel in mode 2 in Supplementary Fig. 36a. Roles are reversed in Supplementary Fig. 36b, where the motion of the colored atoms pairs is antiparallel in mode 1 and parallel in mode 2. Consistent with that, the transmission as well as the propagator $|P^{\beta}_{\mathrm{lr}}(E)|^2$ or $|P^{\gamma}_{\mathrm{lr}}(E)|^2$ are high for $\epsilon_1 < E < \epsilon_2$.

As another example, we classify the interference in phonon transport for the *p*BDA-Br MJ around 6.4 meV. According to Supplementary Fig. 35, a constructive interference is present at that energy that is weakened by asymmetry. The analysis is shown in Supplementary Fig. 37. Three modes contribute significantly. We study the energies $\epsilon_1 < \epsilon_2 < E < \epsilon_3$. Modes 2 and 3 interfere constructively, since mode 2 shows parallel alignment of the displacements for the relevant gold atom pairs, whereas these are aligned antiparallel for mode 3. Modes 1 and 3 on the other hand interfere destructively, since the alignment of both modes is antiparallel. In both cases however, the directions of the displacements for modes 2 and 3 as well as 1 and 3 are slightly different, so that the interferences are weakened (see the discussion of Eq. (12)). This is particularly evident for the gold atom pairs marked in red.

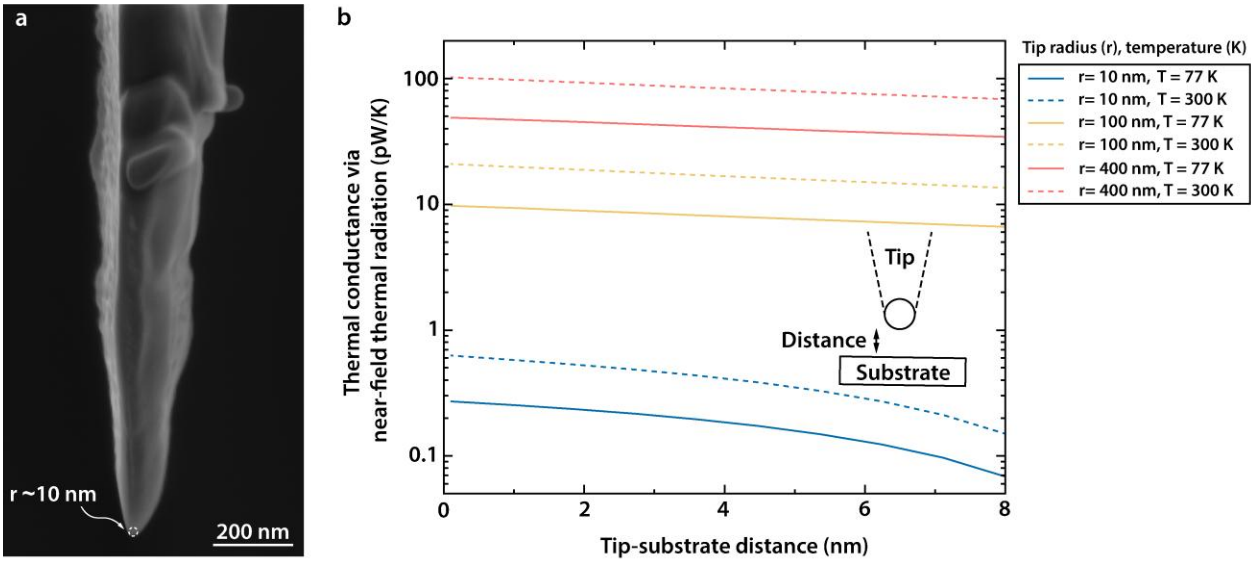

Supplementary Fig. 1 | Estimate of the temperature- and gap-dependent thermal conductance via near-field thermal radiation at sub-10 nm gap sizes using the Derjaguin approximation. a, A scanning electron microscopy (SEM) image of an Au tip attached to the scanning calorimetric probe. The tip radius is estimated to be ~10 nm, as indicated by the white dashed circle overlapped with the tip end. **b**, Computational results of thermal conductance via near-field thermal radiation. The tip radius varies from 10 nm (single crystal Au tip sharpened using a focused ion beam, as shown in panel (a), achieved in this work) to 400 nm (evaporated Au tip using lift-off method, used in other work). Temperature lowering and tip sharpening significantly suppress the near-field thermal radiation between the Au tip and Au substrate, resulting in a negligible influence of near-field radiation on heat transport in single-molecule junctions.

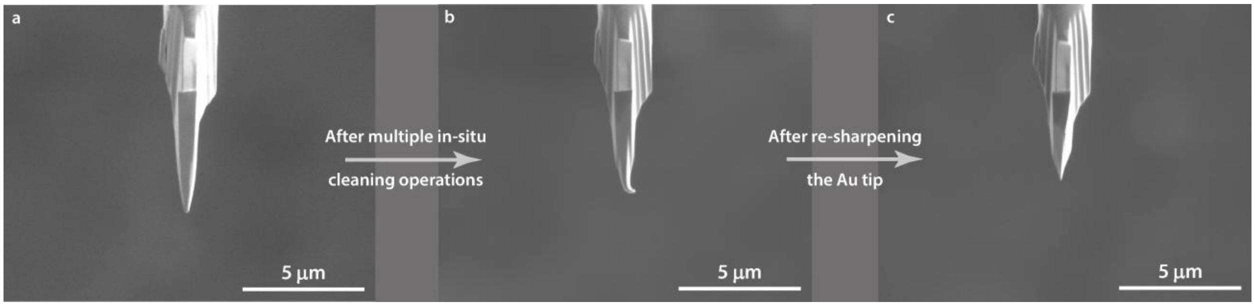

Supplementary Fig. 2 | Scanning electron microscopy images of an Au tip attached to the scanning calorimetric probe. **a**, The tip is sharpened for measurements of single-molecule junctions using a focused ion beam (FIB). **b**, The tip after multiple in-situ cleaning operations. **c**, The same tip after resharpening using a FIB.

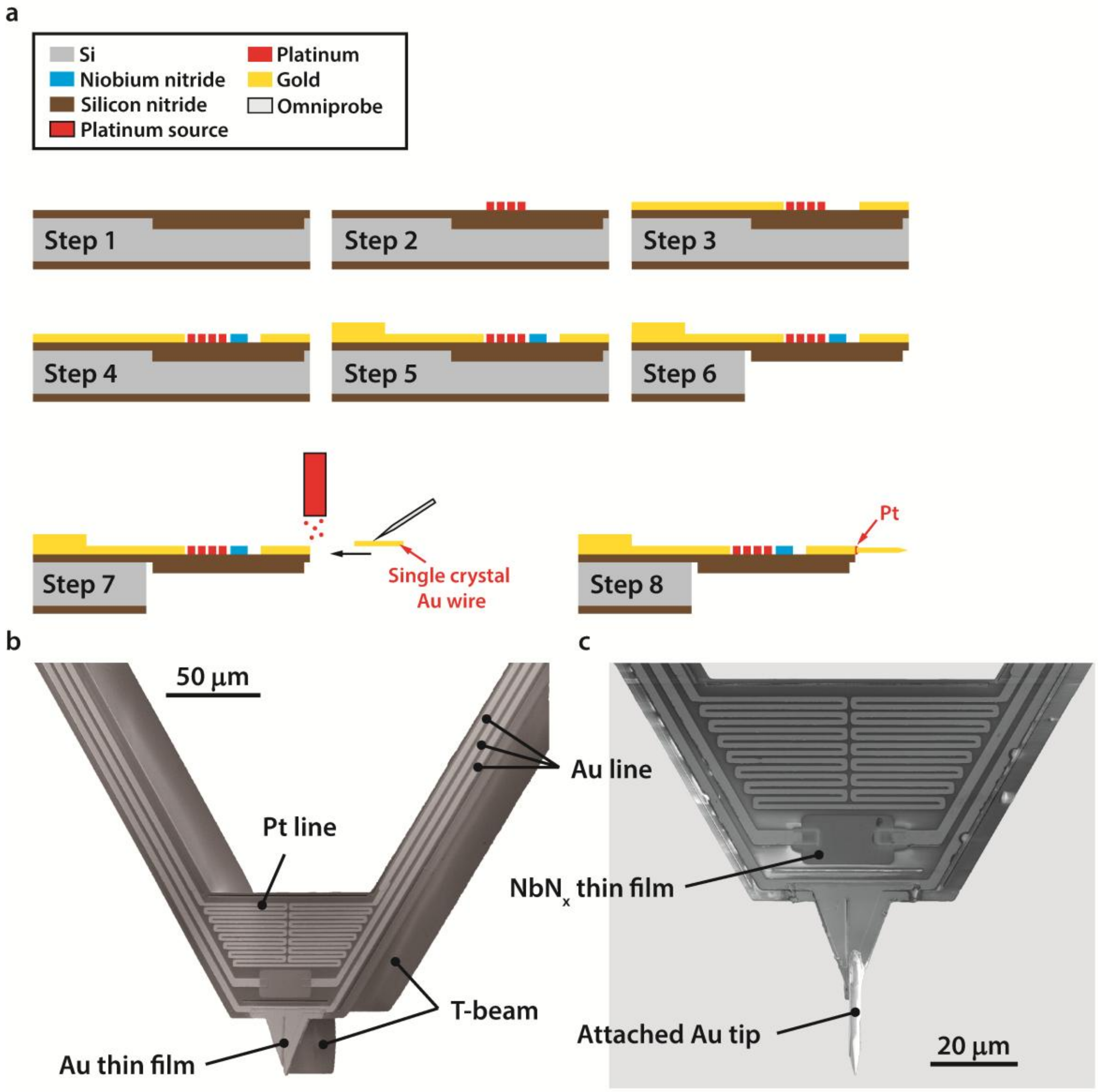

Supplementary Fig. 3 | Fabrication process for the calorimetric scanning probe (CSP). a, Illustration of the fabrication process of the CSP with an attached single crystal Au wire. In step 1**,** The T-beam structure of the CSP was first defined using deep reactive ion etching (DRIE) and then filled with a 600 nm of low-stress silicon nitride film. In steps 2-5, the 30 nm thick platinum line, 70 nm thick Au lead, 100 nm thick niobium nitride film and 500 nm thick Au pad were deposited onto the wafer. Subsequently (step 6), the CSP was released after a backside etch using reactive ion etching (RIE). Next (step 7), a 5-μm-diameter Au crystal wire (99.99% purity) was attached to the distal end of the CSP. Approximately 200 nm thick Pt was in-situ deposited at the junction of the tip and the Au surface to form a good electrical and thermal connection between the Au wire and the CSP. Finally (step 8), the attached Au wire was further sharpened to feature an ~10 nm radius tip. **b**, A scanning electron microscope (SEM) image of the CSP released after step 6. **c**, The zoomed-in SEM image of the CSP, the end of which was attached to an Au tip after step 7. The gray background is introduced to provide better contrast for visualizing the attached Au tip.

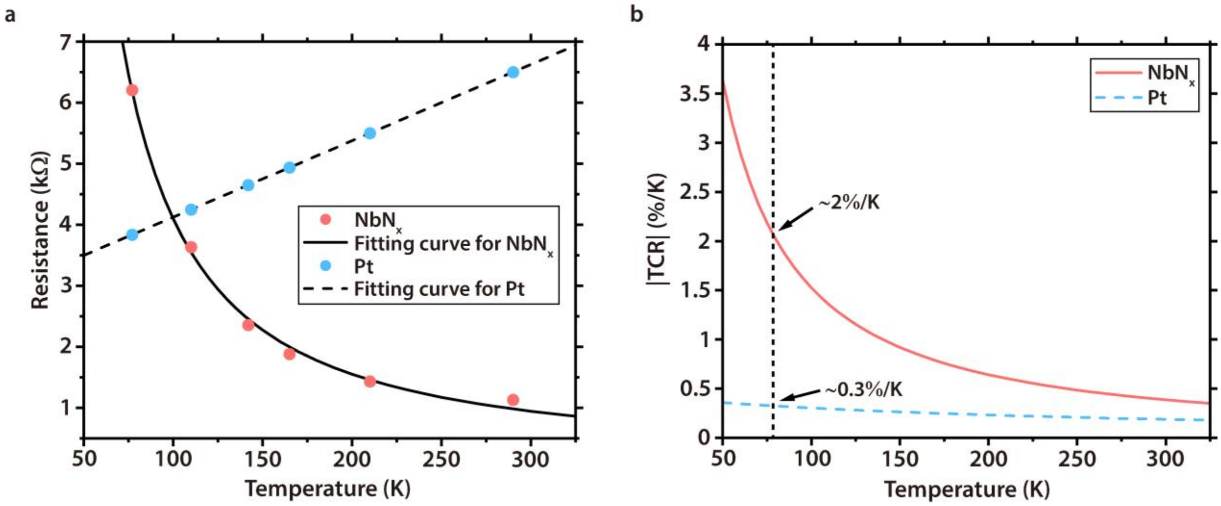

Supplementary Fig. 4 | Characterization of the electrical properties of the NbN$_x$ thin film and the Pt line. a, Measured resistance vs. temperature for the NbN$_x$ thin film and the Pt line. Fits to the measured temperature-dependent resistance were performed following the approaches described in Methods. **b**, The corresponding temperature coefficient of resistance (TCR) obtained from the fitting curves in (**a**) for the NbN$_x$ thin film and the Pt line. At 77 K, the TCR of the NbN$_x$ thin film was ~ –2 %/K, the absolute value of which approximately an order of magnitude higher than the TCR of the Pt line (~0.3 %/K). The uncertainty in the measurements is smaller than the symbol size in panel (**a**).

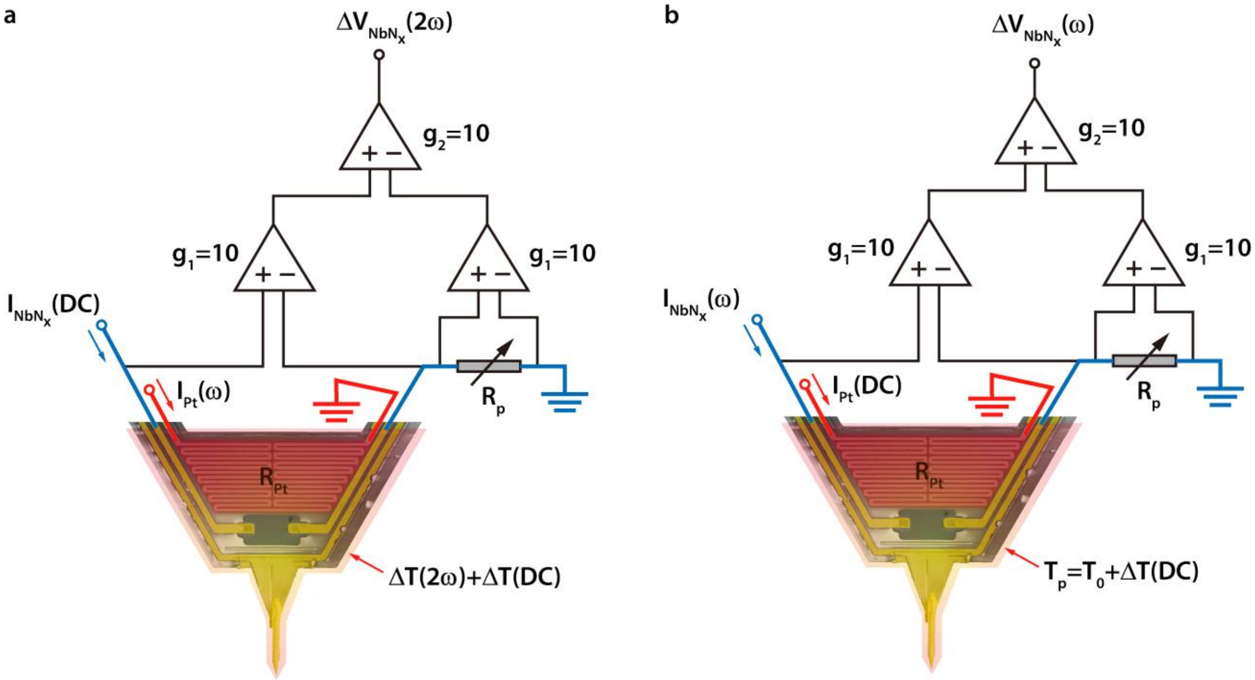

Supplementary Fig. 5 | Measurement schemes for characterizing the thermal response and the thermal conductance of the calorimetric scanning probe (CSP). a, Illustration of the AC heating DC sensing method[36,37]. The integrated Pt line acted as a heater and was supplied with a sinusoidal current, while the NbN_x thin film served as a thermometer and was supplied with a DC current. In this method, the second harmonic of the differential voltage across the NbN_x thin film reflected the second harmonic of the temperature modulation in the CSP (see Methods for details). **b**, Illustration of the DC-heating AC-sensing method[36,37]. The integrated Pt line acted as a heater and was supplied with a DC current, while the NbN_x thin film served as a thermometer and was supplied with a sinusoidal current. In this method (see Methods for details), the first harmonic of the differential voltage across the NbN_x thin film reflected the temperature elevation (i.e., DC component) in the CSP.

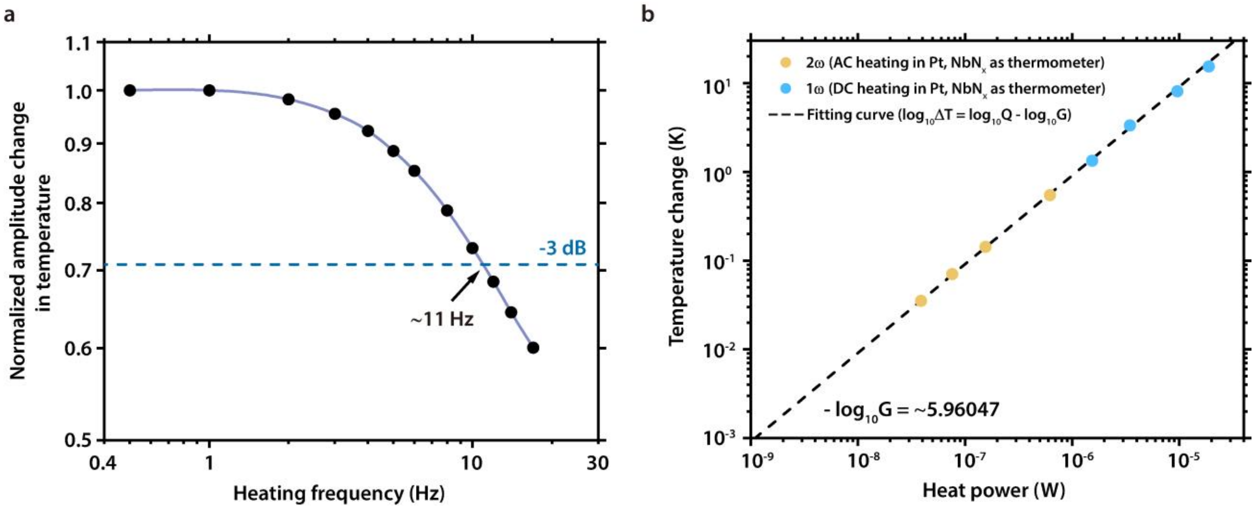

Supplementary Fig. 6 | Thermal characterization of the calorimetric scanning probe (CSP). a, Thermal response of the CSP as a function of heating frequency. The thermal cut-off frequency, corresponding to the frequency at which the amplitude is attenuated to its -3 dB value, is ~11 Hz. The experimental uncertainty is smaller than the symbol size. **b,** Measured temperature change (ΔT) of the CSP vs. input heat power (Q). The data obtained for DC heat inputs is shown in blue dots and the data for AC heat inputs is shown in yellow dots. The thermal conductance of the CSP is extracted from the linear fit to the Q vs. ΔT data and is found to be ~1.1 μW/K.

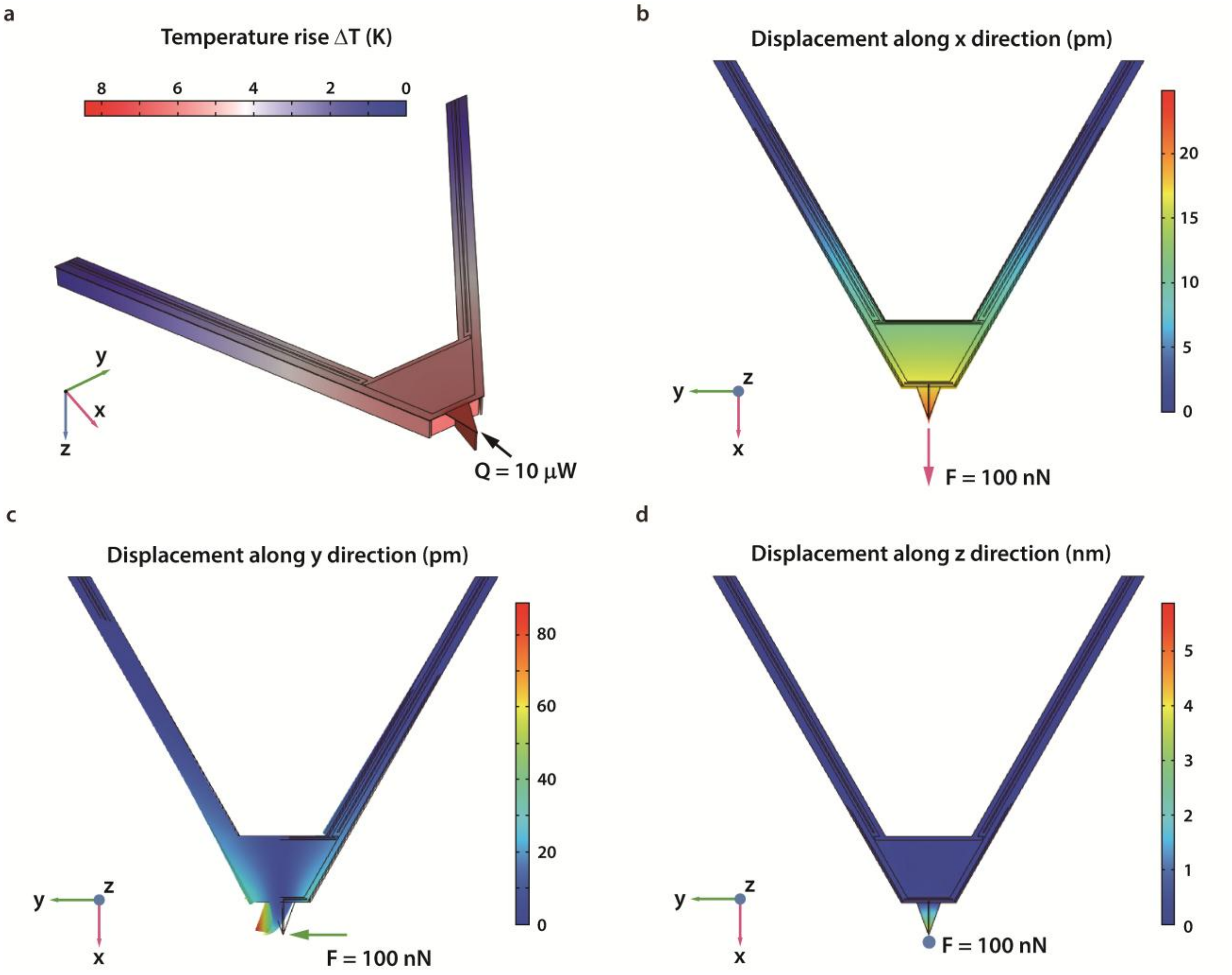

Supplementary Fig. 7 | Estimated thermal conductance and stiffness of the calorimetric scanning probe (CSP) from COMSOL simulations. a, The computed temperature distribution in the probe when a 10 μW heat input is applied to the tip of the CSP. The simulation results indicate that the thermal conductance of the CSP is ~1.2 μW/K. **b**, **c**, **d**, The displacements of the CSP along the *x* (**b**), *y* (**c**), and *z* (**d**) directions when a 100 nN force is applied to the tip of the probe along each respective direction. These results show that the stiffness of the CSP is approximately 4200, 1140, 17.3 N/m along the *x*, *y*, *z* directions, respectively.

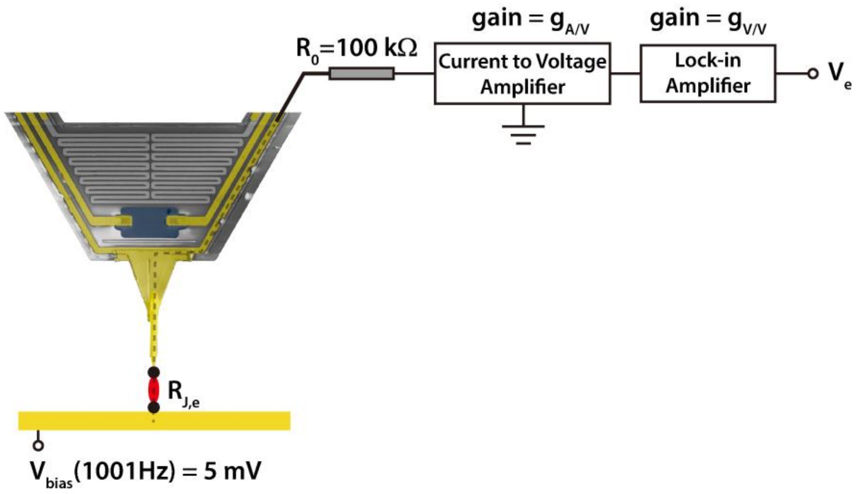

Supplementary Fig. 8 | Illustration of the circuit used to measure the electrical conductance of junctions. To minimize the Joule heat generated by the current passing through the junction, a low-amplitude (5 mV) AC voltage was applied to the bottom electrode, with a 100 kΩ fixed resistor connected in series with the junction. The current signal was converted to a voltage signal using a current-to-voltage amplifier (DLPCA 200). The converted voltage signal was then measured using a lock-in amplifier (SR830, SRS) with a time constant of 10 ms, which corresponds to an equivalent bandwidth of ~15.6 Hz.

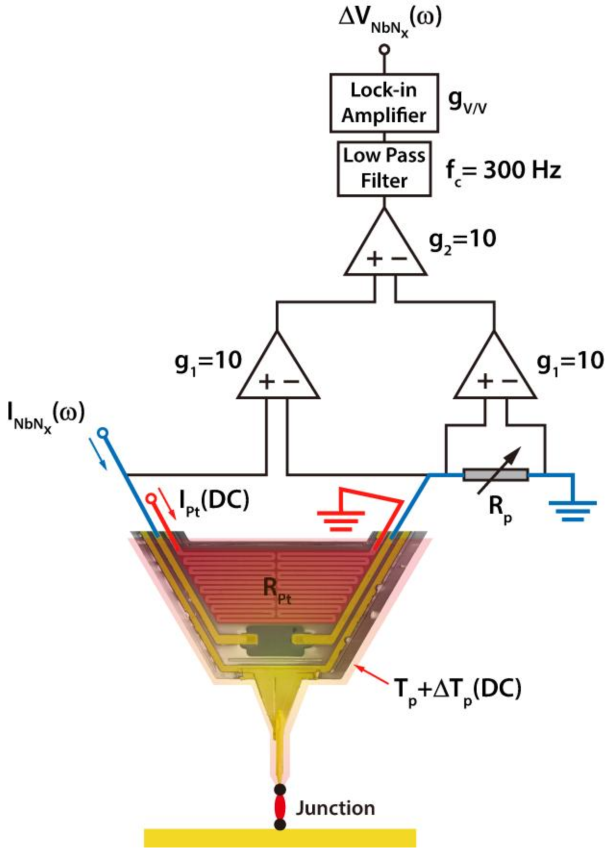

Supplementary Fig. 9 | Schematic description of the setup employed for measuring the thermal conductance of junctions. Schematic of the setup employed for measuring the thermal conductance of junctions using the DC-heating AC-sensing method. The CSP was heated up to ~107 K by applying a large DC current (~110 μA) to the integrated serpentine Pt line. The additional small temperature change (on the order of mK) in the CSP, resulted from the formation, configuration change and rupture of the junctions (i.e., changes in the measured thermal conductance) was reflected in the resistance change in the NbN_x thin film, which was measured using a half-Wheatstone bridge. The voltage output from the bridge was first low-pass filtered using a SR560 voltage amplifier with unity gain and a cut-off frequency of 300 Hz. The filtered signal was then measured using a lock-in amplifier (SR830, SRS) with a time constant of 30 ms, which corresponds to an equivalent bandwidth of ~5.2 Hz.

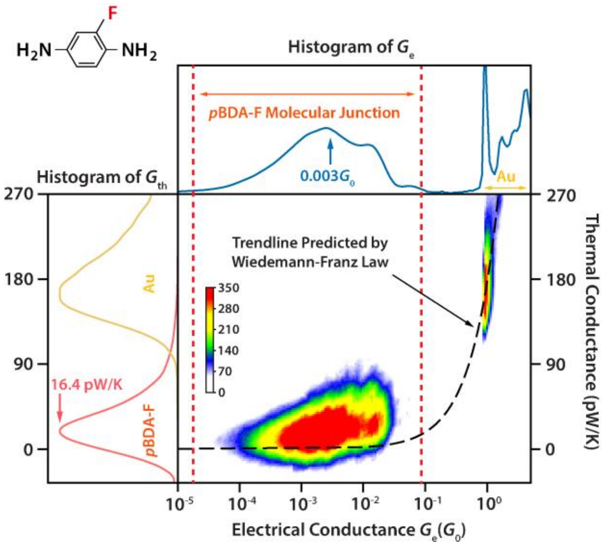

Supplementary Fig. 10 | 2D histogram of the electrical and thermal conductance of *p*BDA-F molecular junctions. The results show that the most probable electrical and thermal conductance of *p*BDA-F molecular junctions were ~0.003 G_0 and ~16.4 pW/K, respectively.

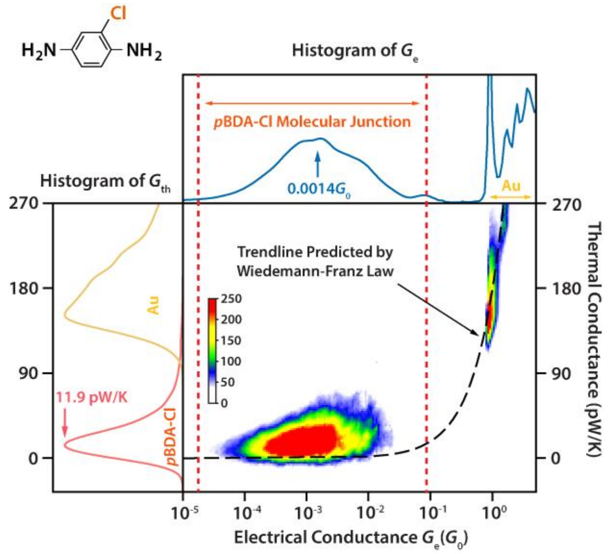

Supplementary Fig. 11 | 2D histogram of the electrical and thermal conductance of *p*BDA-Cl molecular junctions. The results show that the most probable electrical and thermal conductance of *p*BDA-Cl molecular junctions were ~0.0014 G_0 and ~11.9 pW/K, respectively.

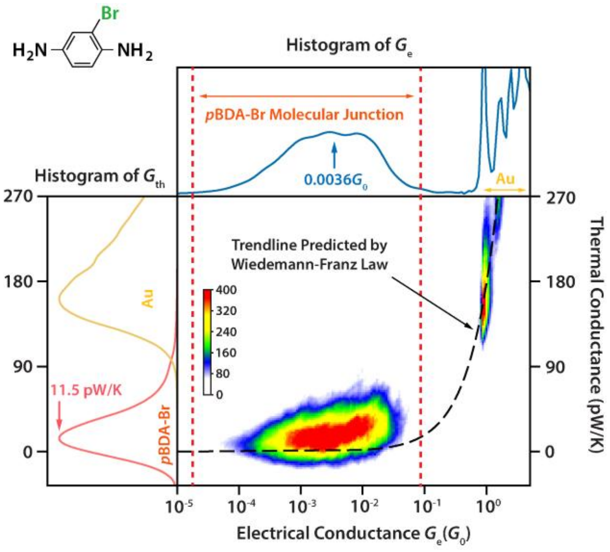

Supplementary Fig. 12 | 2D histogram of the electrical and thermal conductance of *p*BDA-Br molecular junctions. The results show that the most probable electrical and thermal conductance of *p*BDA-Br molecular junctions were ~0.0036 G_0 and ~11.5 pW/K, respectively.

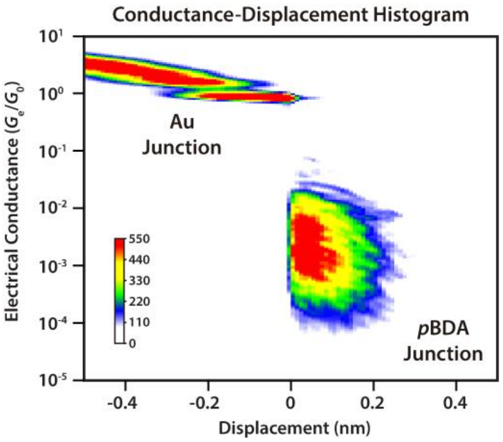

Supplementary Fig. 13 | 2D conductance-displacement histogram of *p*BDA molecular junctions. At 77 K, the single Au atomic junction (G_e at ~1G_0) and single *p*BDA junction can be stretched by ~0.2 nm. The measured electrical conductance of the molecular junctions ranges from ~10^{-4} G_0 to 10^{-2} G_0.

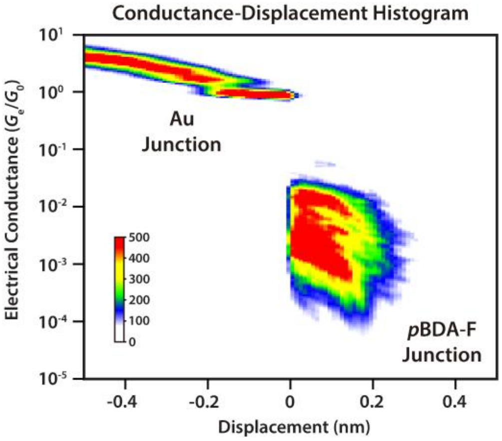

Supplementary Fig. 14 | 2D conductance-displacement histogram of *p*BDA-F molecular junctions. At 77 K, the single Au atomic junction (G_e at ~1G_0) and single *p*BDA-F junction can be stretched by ~0.2 nm. The measured electrical conductance of the molecular junctions ranges from ~10^{-4} G_0 to 10^{-2} G_0.

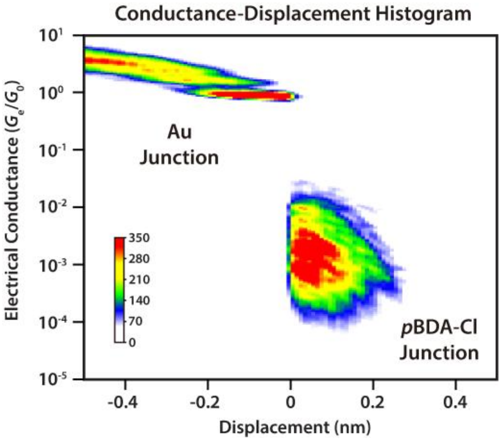

Supplementary Fig. 15 | 2D conductance-displacement histogram of *p*BDA-Cl molecular junctions. At 77 K, the single Au atomic junction (G_e at ~1G_0) and single *p*BDA-Cl junction can be stretched by ~0.2 nm. The measured electrical conductance of the molecular junctions ranges from ~10^{-4} G_0 to 10^{-2} G_0.

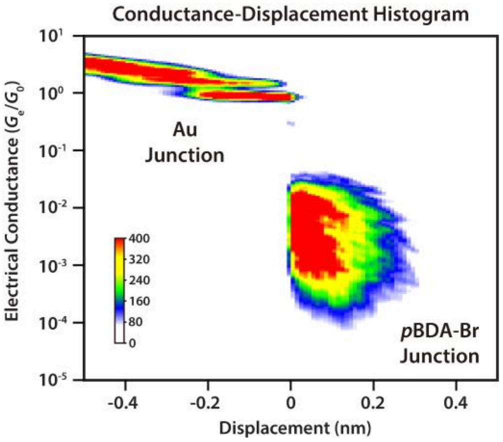

Supplementary Fig. 16 | 2D conductance-displacement histogram of *p*BDA-Br molecular junctions. At 77 K, the single Au atomic junction (G_e at ~1G_0) and single *p*BDA-Br junction can be stretched by ~0.2 nm. The measured electrical conductance of the molecular junctions ranges from ~10^{-4} G_0 to 10^{-2} G_0.

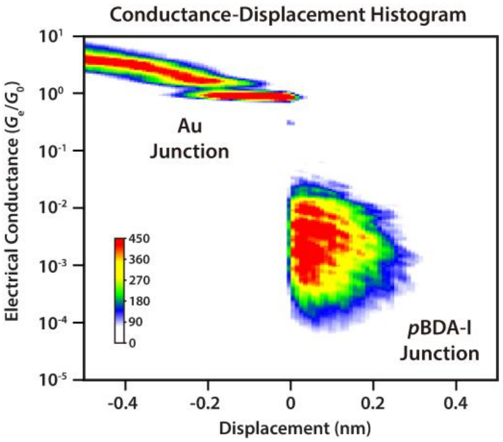

Supplementary Fig. 17 | 2D conductance-displacement histogram of *p*BDA-I molecular junctions. At 77 K, the single Au atomic junction (G_e at ~$1G_0$) and single *p*BDA-I junction can be stretched by ~0.2 nm. The measured electrical conductance of the molecular junctions ranges from ~10^{-4} G_0 to 10^{-2} G_0.

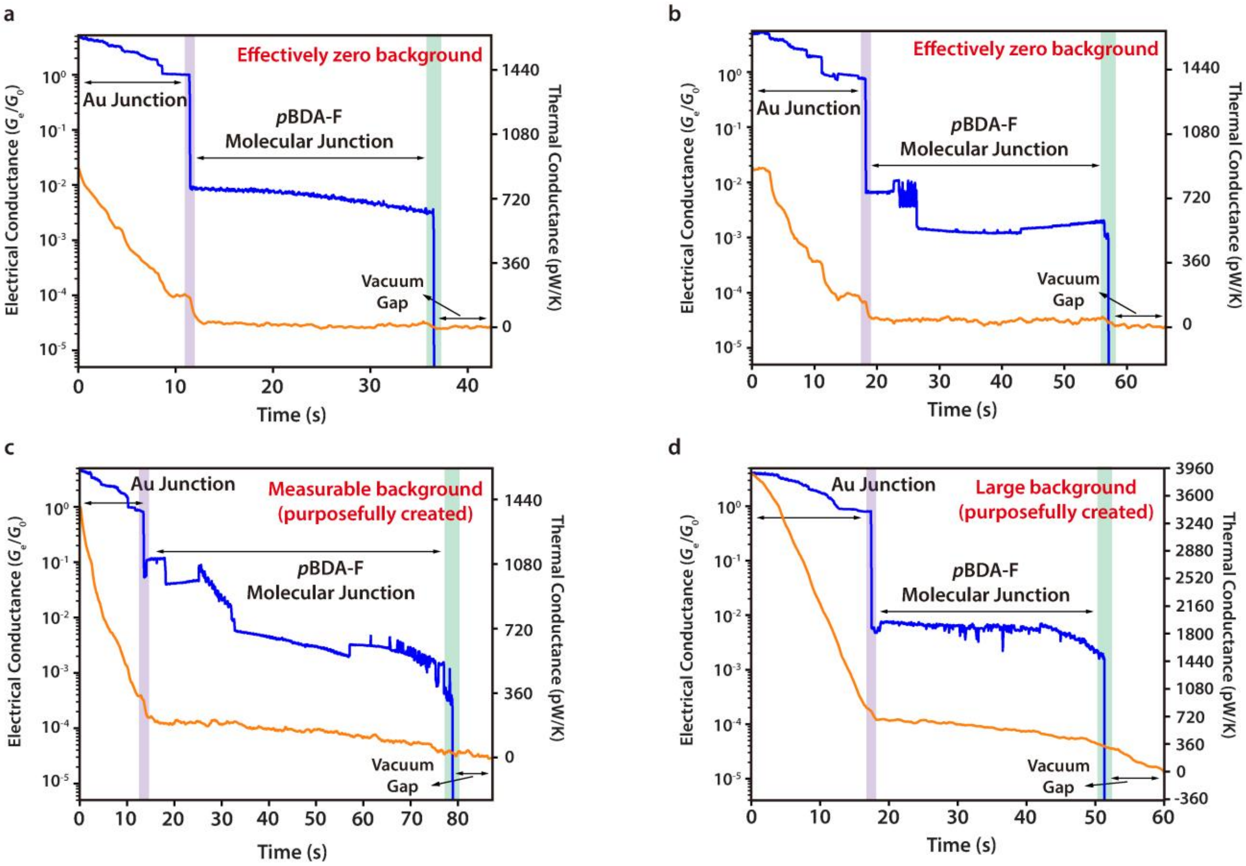

Supplementary Fig. 18 | Comparison of traces with and without thermal background conductance. a, b, Two representative traces for the measured electrical and thermal conductance of Au atomic junctions and *p*BDA-F molecular junctions with zero (negligible) background thermal conductance. **c**, A typical trace found in the measurements when the surface has a measurable background conductance (~10s of pW/K). When such background conductance is present (likely indicating the presence of adsorbed molecules like water), the measured thermal conductance of the molecular junction showed a non-negligible change with respect to time (it can be seen that the thermal conductance gradually reduces with time). The typical step-wise change in the thermal conductance of Au atomic junctions is also smoothened out. **d**, A representative trace for the measurements when the surface features a large background conductance (~few hundred pW/K). Under these conditions the thermal conductance steps associated with the Au junctions are no longer discernable. Similarly, the molecular thermal conductance also features strong time and displacement dependence, like to the varying contribution from the background.

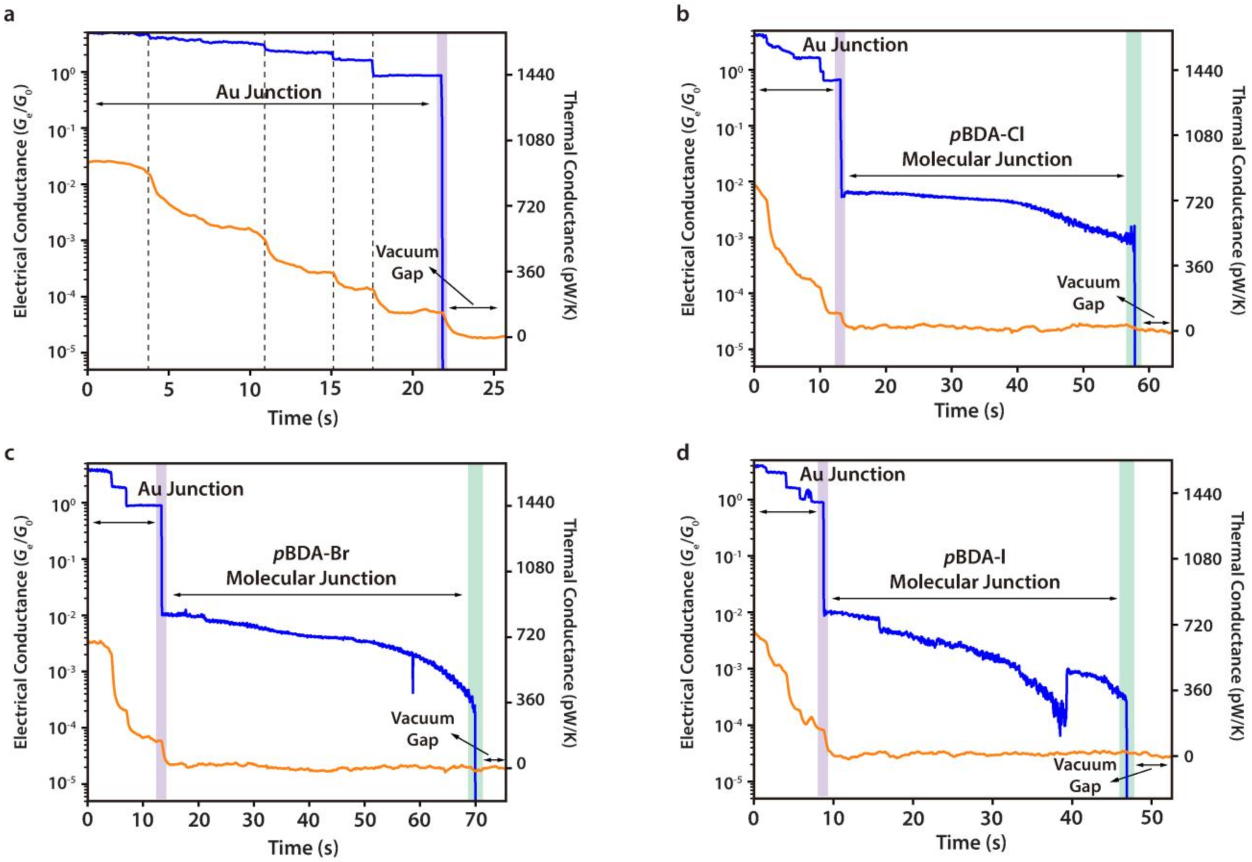

Supplementary Fig. 19 | Characteristics of traces with zero background thermal conductances. a, A representative trace for the measured electrical and thermal conductance of Au atomic junctions obtained from measurements on a clean Au surface. Results show that, synchronized with the measured electrical conductance, the measured thermal conductance also exhibited a clear step-wise change, which was relatively smooth compared to the abrupt changes in the electrical conductance likely due to the thermal response of the calorimetric scanning probe (CSP) and the applied moving average (see Section 7 for details). **b**, **c**, **d**, Representative traces for the measured electrical and thermal conductance of *p*BDA-Cl (**b**), *p*BDA-Br (**c**), *p*BDA-I (**d**), respectively. These traces feature an instantaneous drop in electrical conductance (see the region highlighted in green) when the molecular junction ruptures and are representative of those used in our averaging scheme.

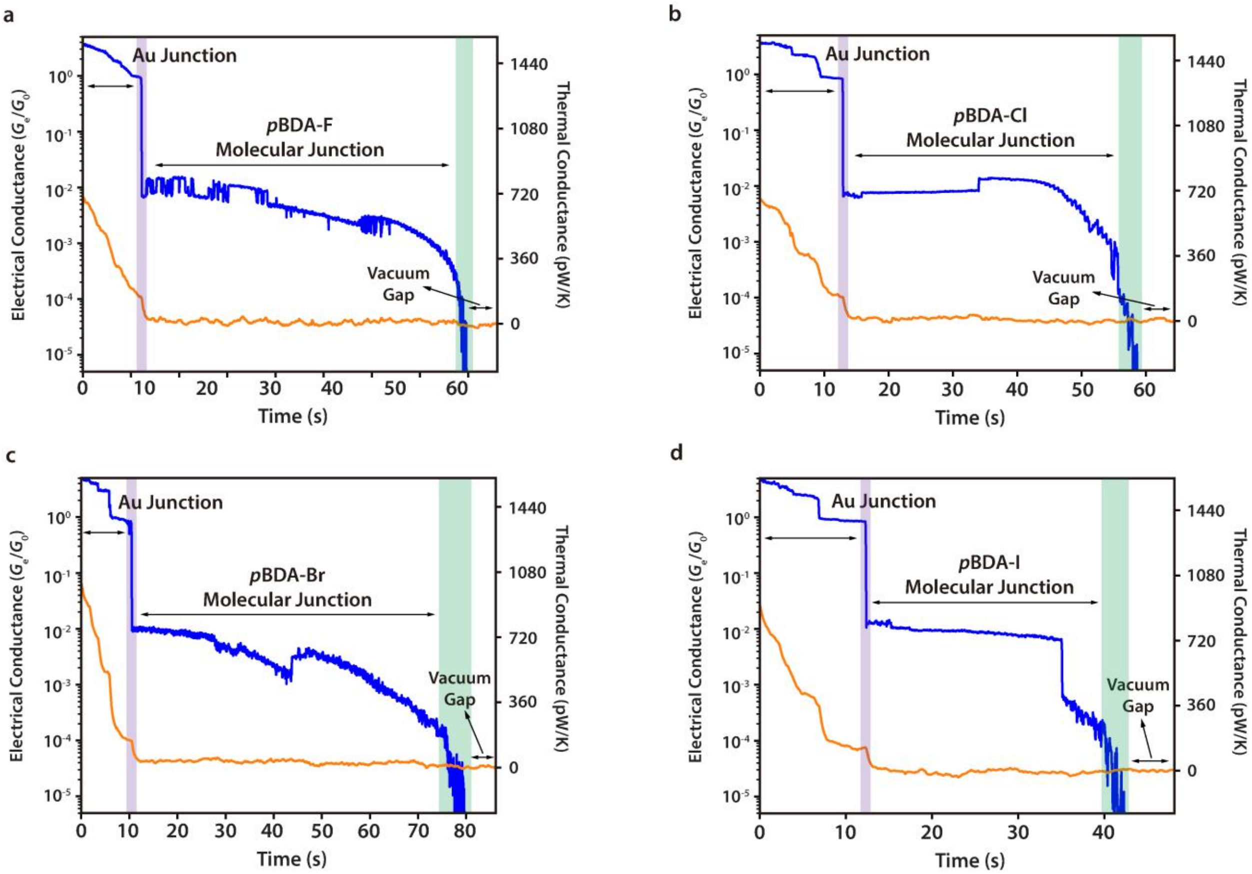

Supplementary Fig. 20 | Characteristics of traces that do not feature an abrupt change in electrical conductance during rupture. a, b, c, d, Representative traces collected in the measurements of *p*BDA-F (**a**), *p*BDA-Cl (**b**), *p*BDA-Br (**c**), and *p*BDA-I (**d**) molecular junctions. As seen, the measured electrical conductance does not change abruptly when the molecular junction ruptures (see the region highlighted in green), which is in contrast to the behavior of the junctions shown in Supplementary Fig. 19. The measured thermal conductance showed a step wise change when Au junctions ruptured. When the molecular junctions were formed and stretched, the measured thermal conductance was nearly displacement-independent. These traces were used only for the histogram analysis due to the difficulty in determining and aligning the rupture point of molecular junctions in these traces.

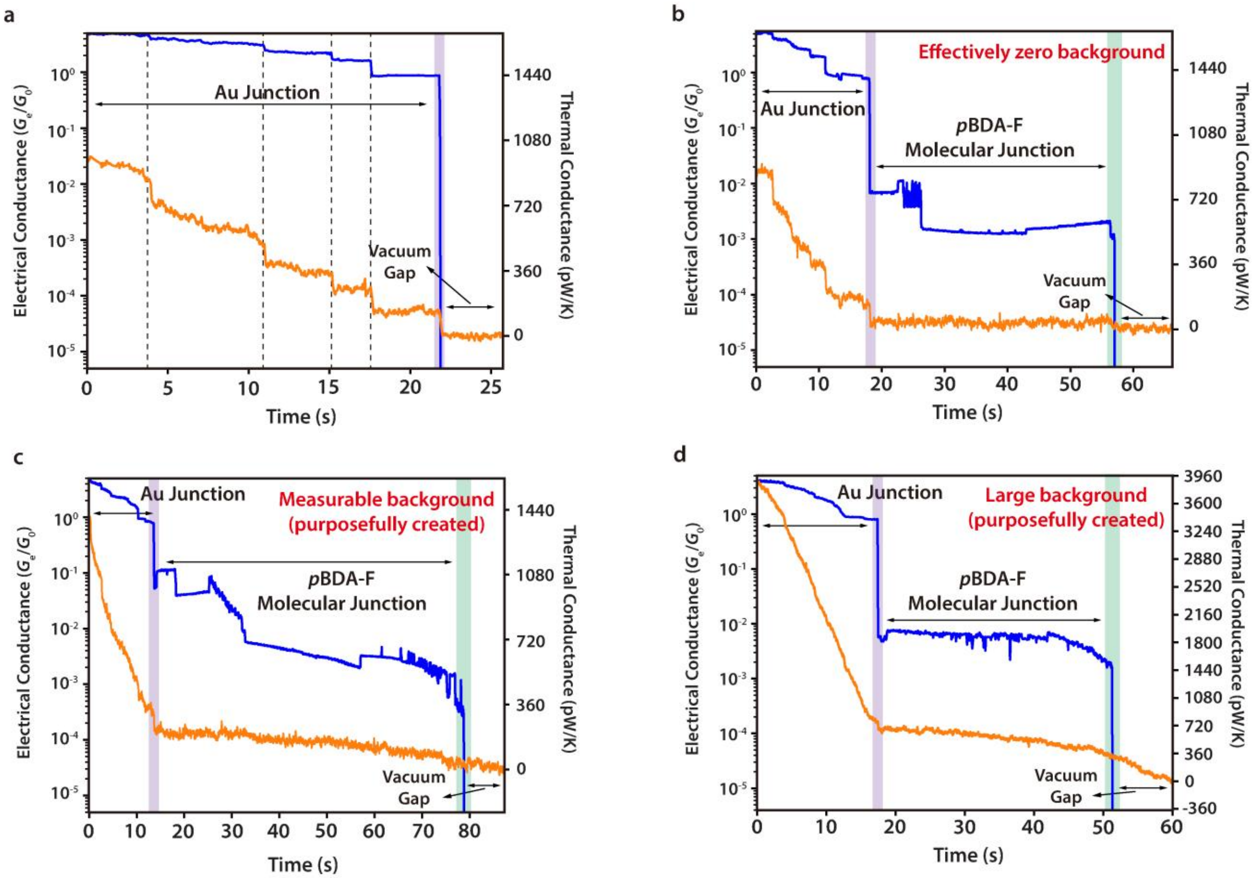

Supplementary Fig. 21 | Traces plotted using raw data without a moving average. a, The trace has the same data as in Supplementary Fig. 19a but without performing a moving average. **b**, The trace has the same data as in Supplementary Fig. 18b but without performing a moving average. **c,** The trace has the same data as in Supplementary Fig. 18c but without performing a moving average. **d**, The trace has the same data as in Supplementary Fig. 18d but without performing a moving average. We note that the moving average was only applied to the thermal conductance signal. The moving average was optimized (~1000 points) to ensure that the original observed features shown in the raw data such as the stepwise change in the measure thermal conductance are still visible.

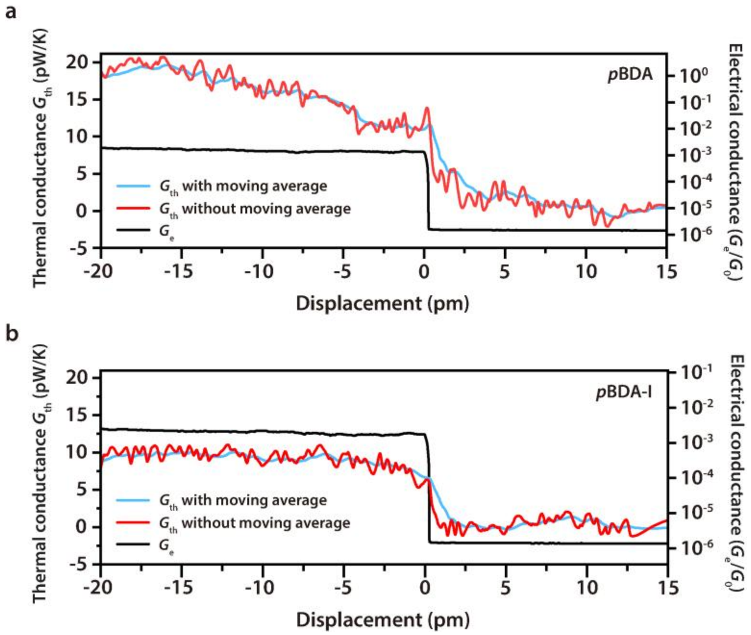

Supplementary Fig. 22 | Comparison of thermal conductance traces obtained using the rupture point analysis with and without a moving average. Employing a moving average does not affect the observed trends or key conclusions.

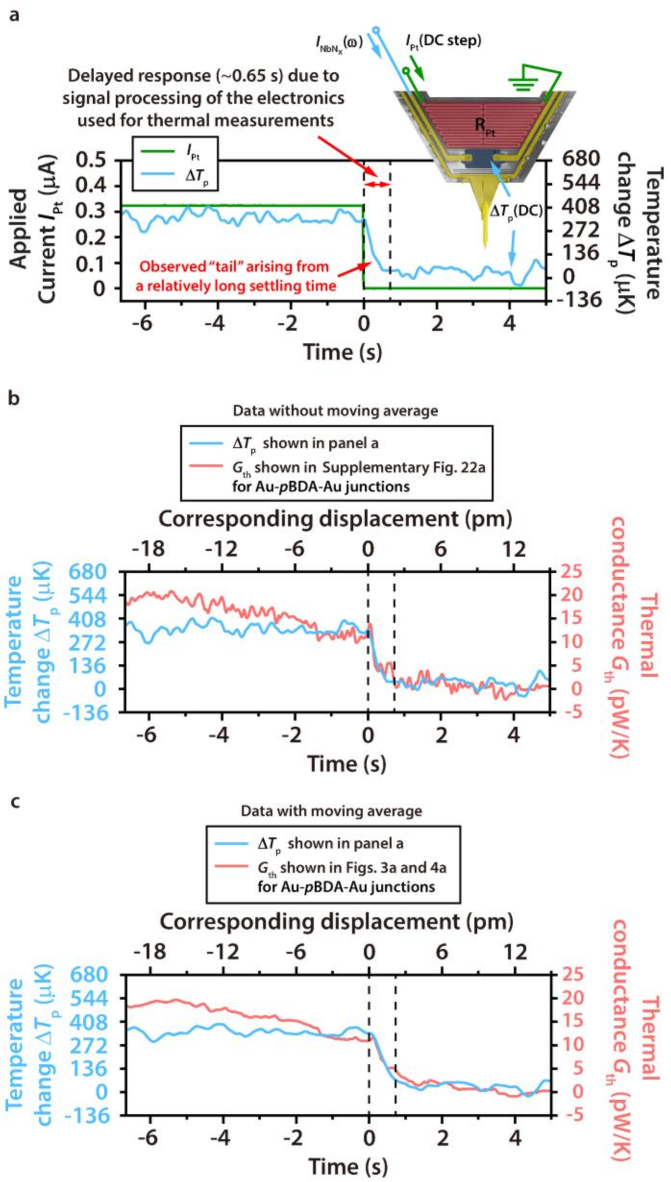

Supplementary Fig. 23 | Characterization of the settling time in our thermal measurements. **a**, Thermal response of the probe to a step change in the heat input. In this control experiment a small electrical current (green curve) is applied to the probe's integrated Pt line and the induced temporal response of temperature change of the probe (blue curve) is measured using the NbN_x thermometer. The long red arrow points to the "tail", which is also present in the curves for the measured thermal conductance of single-molecule junctions shown in Figs. 3a, 3b and 4a. **b**, Comparison of the data for Au-*p*BDA-Au junctions shown in Fig. 22a (red curve) and the data shown in panel (a) (blue curve) without performing a moving average. **c**, Comparison of the data for Au-*p*BDA-Au junctions shown in Fig. 22a (blue curve) and the data shown in panel (a) (blue curve) with a moving average. These results indicate that the observed "tail" is due to the relatively long settling time arising from the signal conditioning in electronics required to resolve the minute thermal signals.

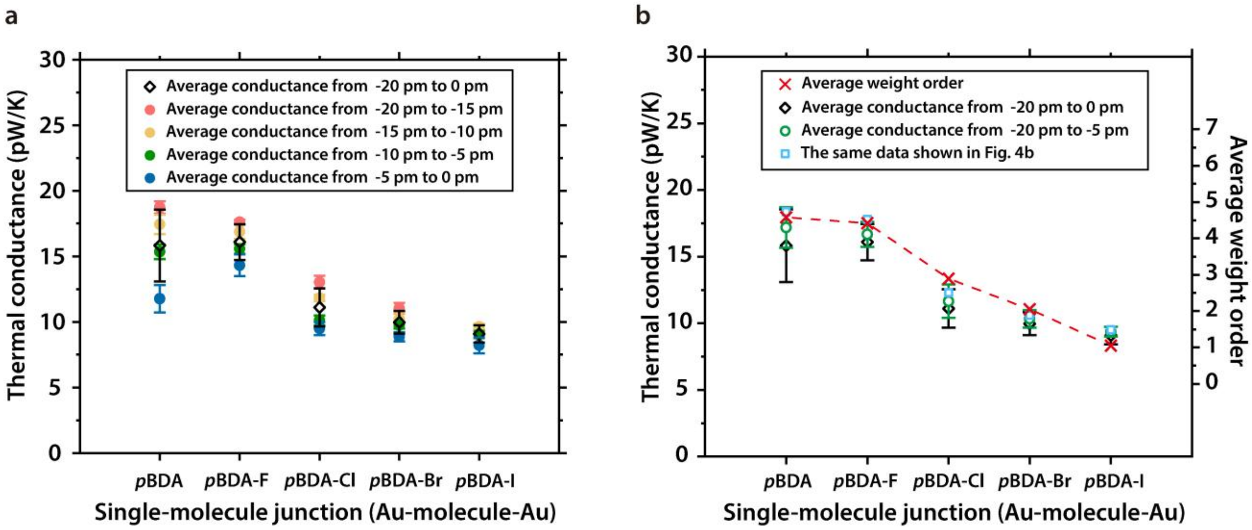

Supplementary Fig. 24 | Additional analysis to support the robustness of the conclusions drawn from Fig. 4b. a, The thermal conductance of single molecule junctions, obtained from the rupture point analysis using data from different displacement ranges. **b**, Results from the statistical analysis of the data from -20 pm to 0 pm by assigning weights to the data in several intervals (see detailed explanation in section 7). These results support the conclusion that the thermal conductances of pBDA-derived junctions follow pBDA (or pBDA-F) > pBDA-Cl > pBDA-Br > pBDA-I.

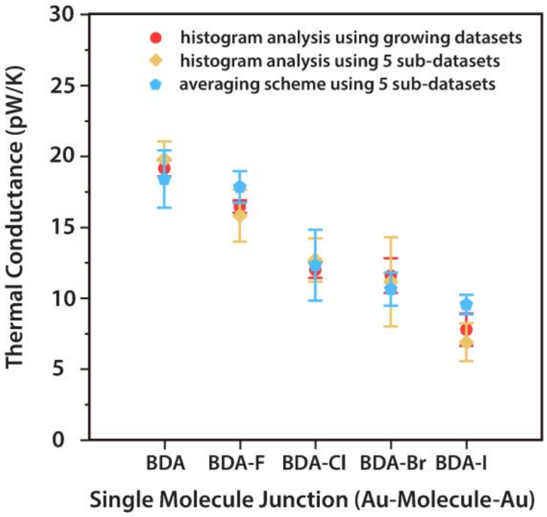

Supplementary Fig. 25 | Analysis of experimental uncertainty in the thermal conductance of single molecule junctions. The measured thermal conductance of *p*BDA and its derivative junctions shows good agreement across the three different data analyses. It is evident that the measured difference in the thermal conductance of these molecular junctions result from the introduction of substituents.

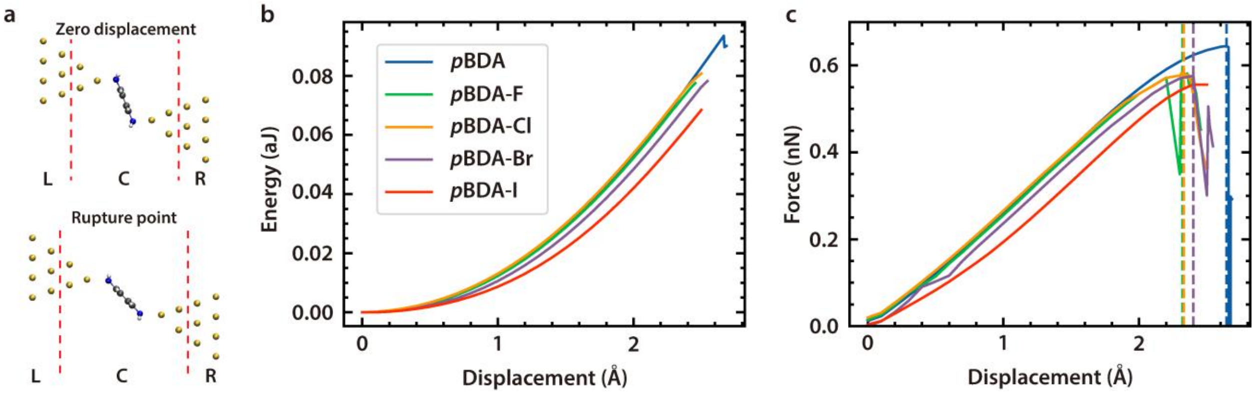

Supplementary Fig. 26 | Junction geometries and stretching procedure. **a**, Geometry of a *p*BDA MJ at zero displacement (upper panel) and at the rupture point (lower panel). The figures also show, how the extended central cluster (ECC) is partitioned into left (L), central (C) and right (R) parts. **b**, Calculated total DFT energy of all MJs used in this work. **c**, Force derived from the curves in panel (b) by numerical differentiation. Dashed lines indicate the displacements with the maximum force, which define the breaking point.

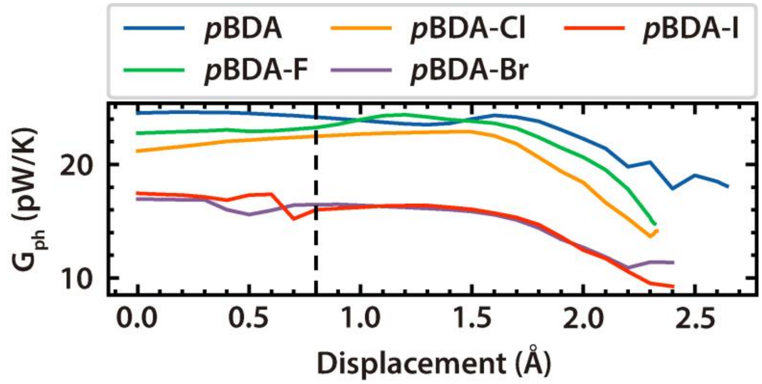

Supplementary Fig. 27 | Displacement-dependent thermal conductance. Thermal conductance, plotted against electrode displacement, is calculated at a temperature of T = 92 K. The thermal conductance of each MJ is shown from zero displacement (see Supplementary Fig. 26) to the rupture point. The black line marks the displacement, at which the MJs are analyzed in Fig. 5 of the main manuscript.

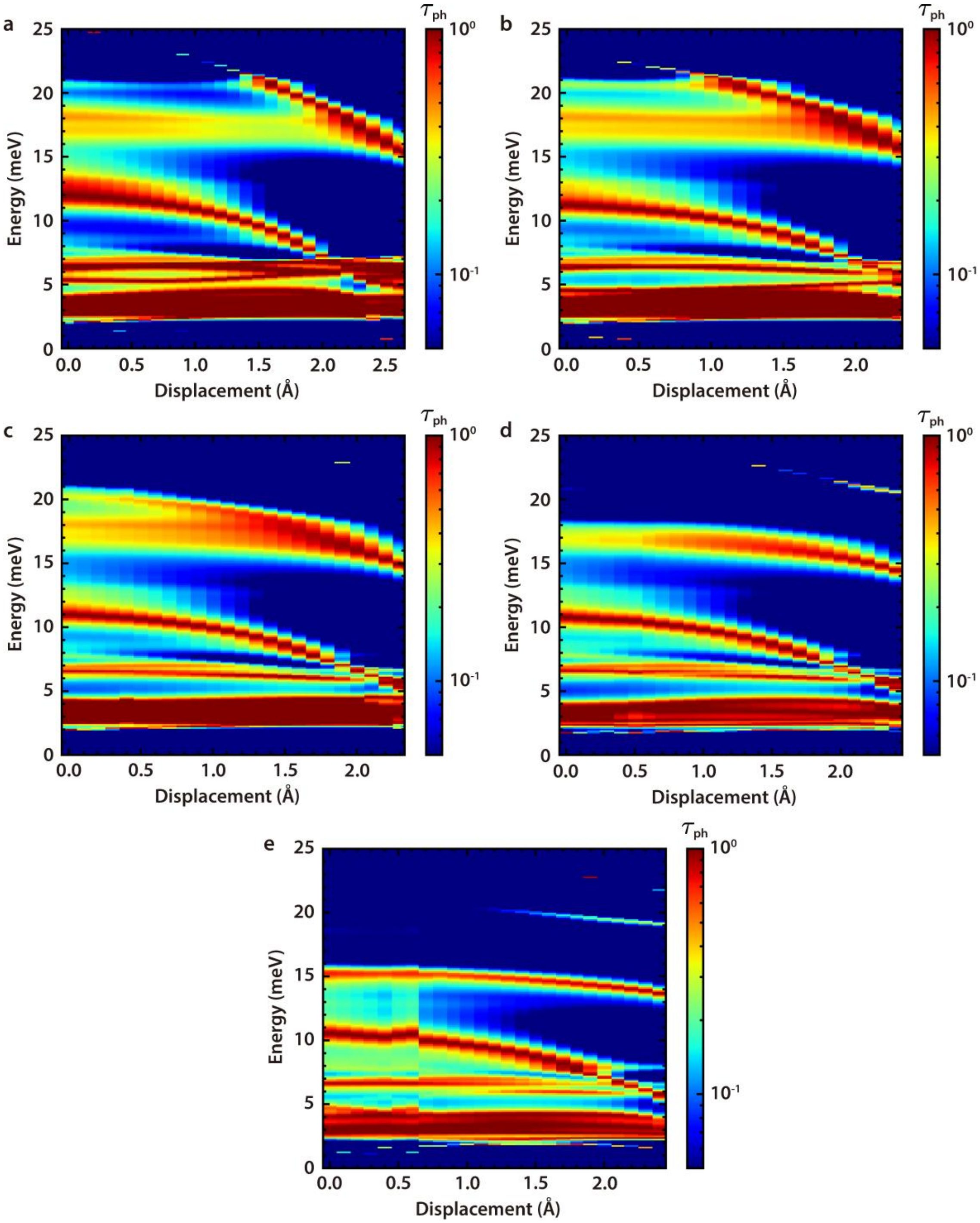

Supplementary Fig. 28 | Phonon transmission maps. a, Phonon transmission for the *p*BDA MJ as a function of energy and displacement. The transmission is encoded according to the colorbar on the right of each panel, and displacements reach from zero to the rupture point. **b, c, d, e,** Same as panel (a) but for *p*BDA-F, *p*BDA-Cl, *p*BDA-Br, and *p*BDA-I MJs, respectively.

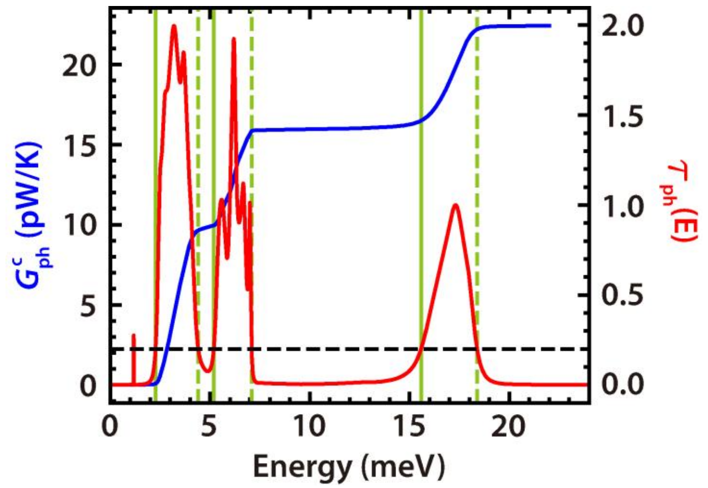

Supplementary Fig. 29 | Analysis of the cumulative thermal conductance. The cumulative thermal conductance (blue) is plotted along with the phonon transmission (red) as a function of energy for the *p*BDA MJ at zero displacement. The black horizontal line at a phonon transmission of 0.2 defines the threshold used in the analysis. Three regions with significant contributions to the cumulative thermal conductance of 9.6 pW/K, 5.9 pW/K and 5.7 pW/K from 2.3 to 4.4 meV, 5.2 to 7.1 meV and 15.6 to 18.4 meV, respectively, are identified. The background contribution is 1.2 pW/K, and the total thermal conductance is 22.4 pW/K.

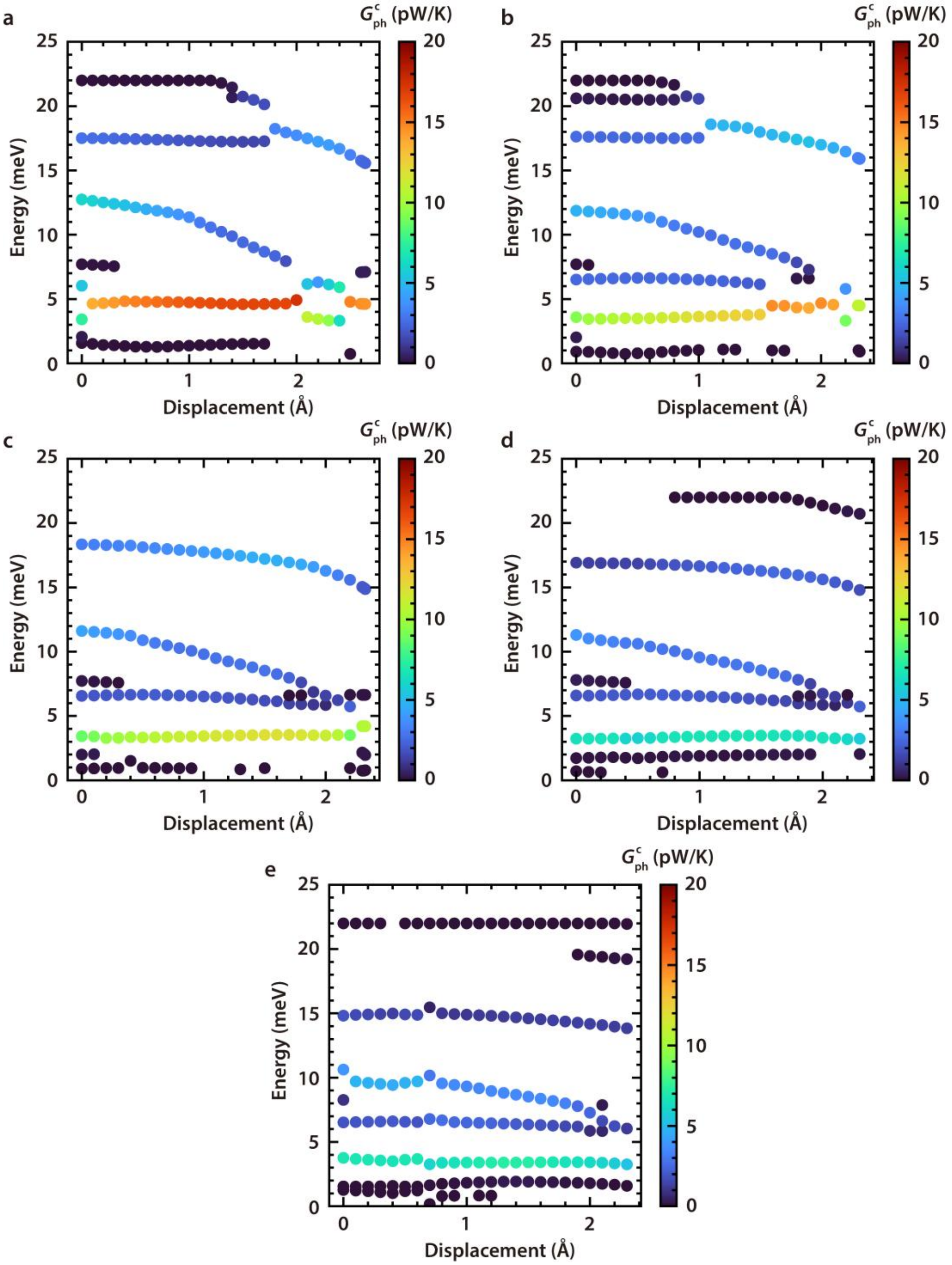

Supplementary Fig. 30 | Cumulative thermal conductance as function of energy and displacement. a, Cumulative thermal conductance of the *p*BDA MJ. At a fixed displacement, points identify regions that yield a significant contribution to the cumulative thermal conductance. The size of the contribution is encoded in the point's color. The data is extracted with the method, illustrated in Supplementary Fig. 29. Displacements are shown from zero up to the rupture point. **b, c, d, e,** Same as panel (a) but for *p*BDA-F, *p*BDA-Cl, *p*BDA-Br, and *p*BDA-I MJs, respectively.

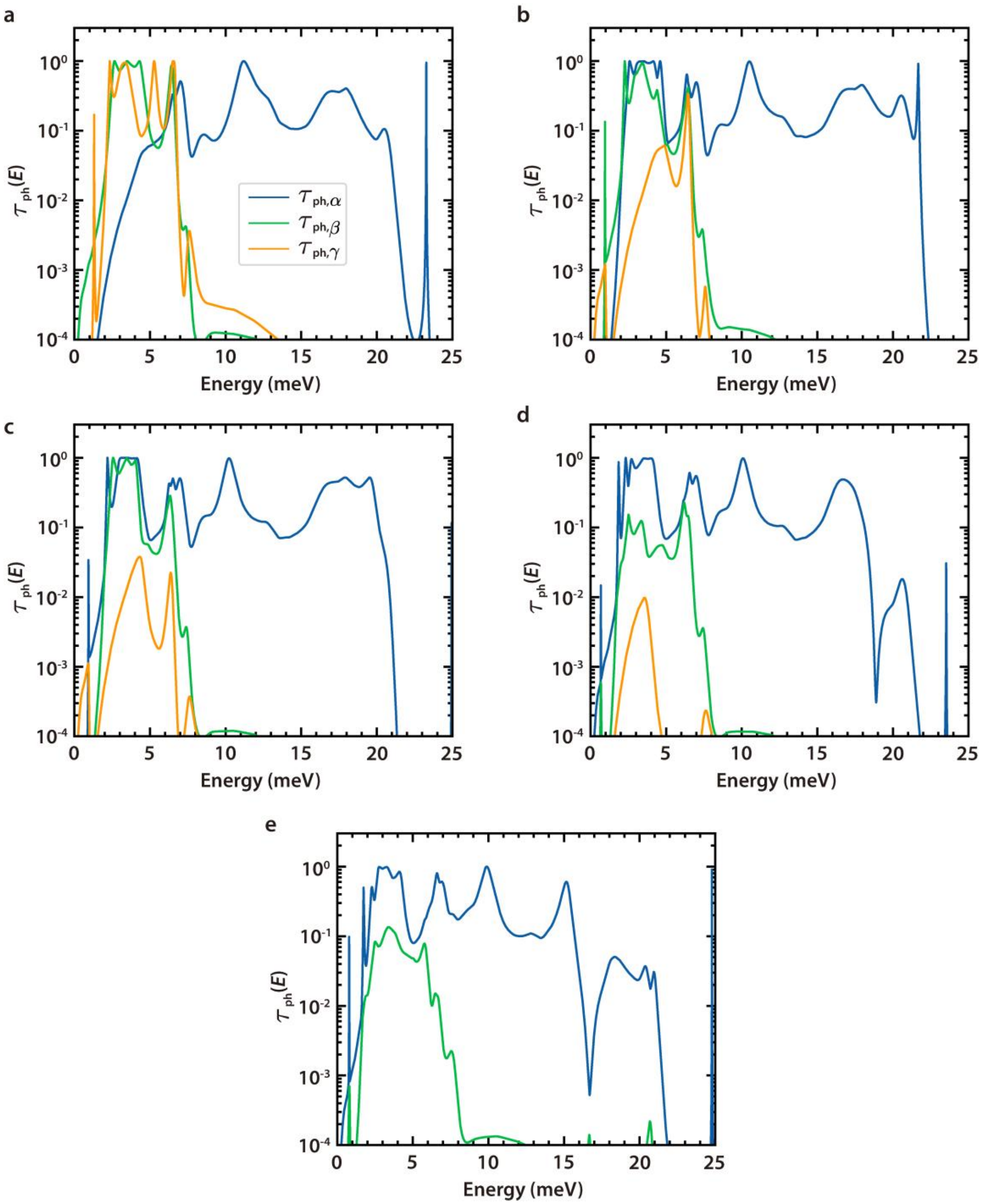

Supplementary Fig. 31 | Eigenchannel-resolved phonon transmission. a, Phonon transmission as a function of energy, resolved into the TE contributions $\tau_{\mathrm{ph},\alpha}(E)$, $\tau_{\mathrm{ph},\beta}(E)$, $\tau_{\mathrm{ph},\gamma}(E)$ for the junction geometries at $d = 0.8$ Å. The ordering is performed according to the values of $\tau_{\mathrm{ph},\mu}$(18 meV), and the TEs are traced based on their wavefunctions. **b**, **c**, **d**, **e**, Same as panel (a) but for *p*BDA-F, *p*BDA-Cl, *p*BDA-Br and *p*BDA-I MJs.

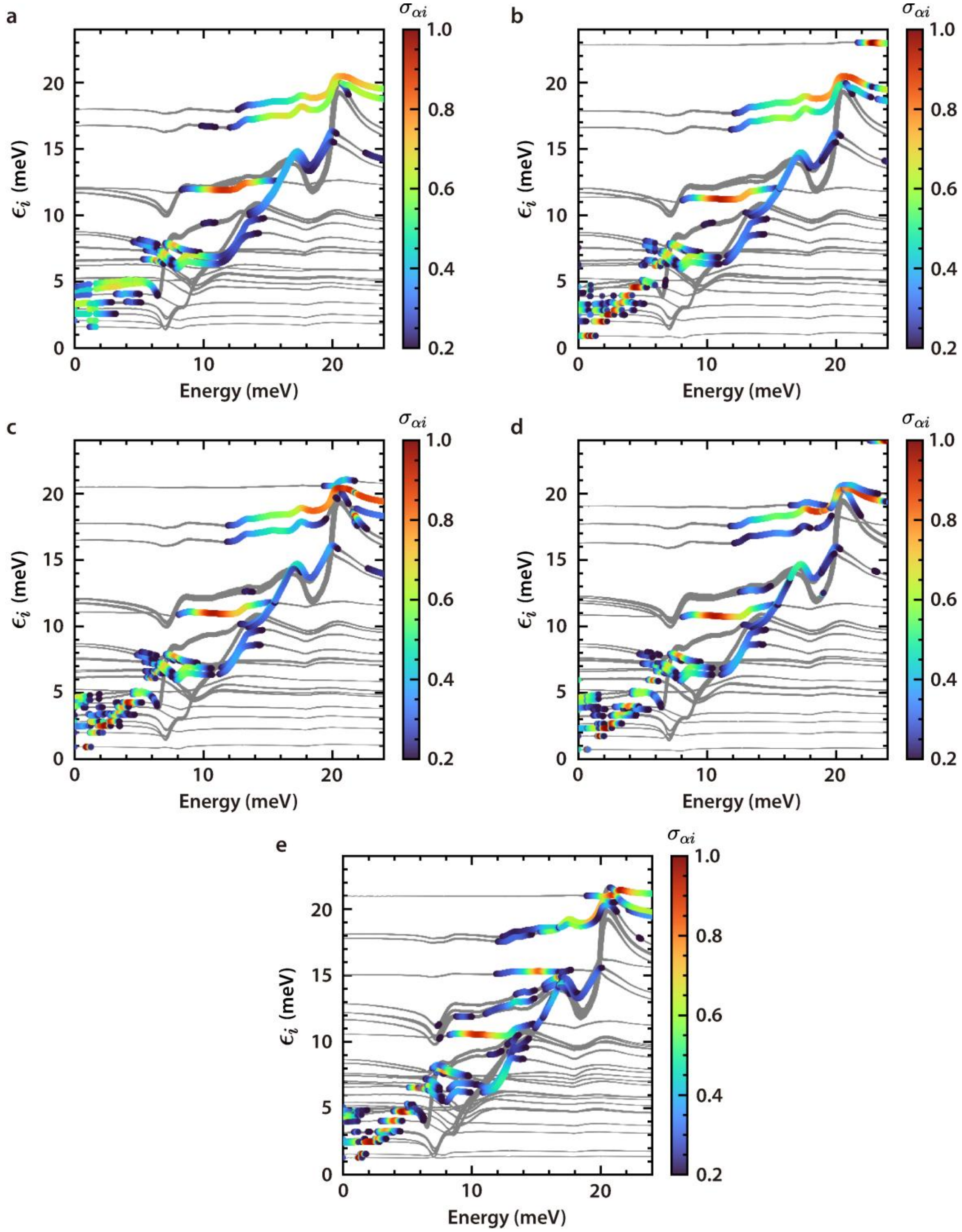

Supplementary Fig. 32 | Overlap of TEs and vibrational eigenmodes. a, Decomposition of the TE α of the *p*BDA MJ at displacement $d = 0$ Å into eigenmodes of the extended central cluster, including the embedding self-energies. The width of the grey lines encodes the broadening of the eigenmodes with energies ε_i by the embedding self-energies. The overlap $\sigma_{\alpha i}$ of the eigenmode i and the TE α is visualized by color. Overlaps below a threshold of $\sigma_{\alpha i} < 0.2$ are not shown. **b**, **c**, **d**, **e**, Same as panel (a) but for the *p*BDA-F, *p*BDA-Cl, *p*BDA-Br and *p*BDA-I MJs, respectively.

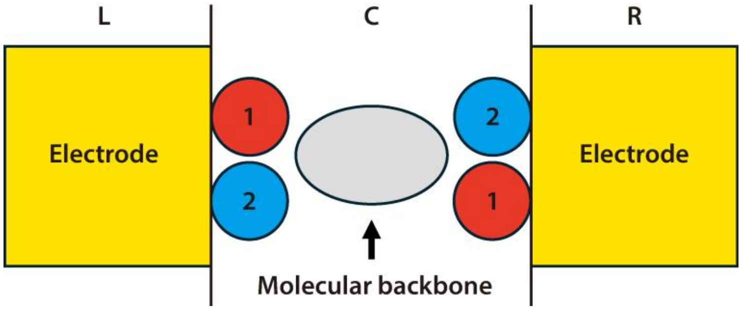

Supplementary Fig. 33 | Model for phonon interference in two dimensions. Colored circles represent the atoms of the central part that are coupled to the left or right electrodes. The colors indicate the point symmetry, which is present in our three-dimensional transport calculations and is exploited for explaining the interference.

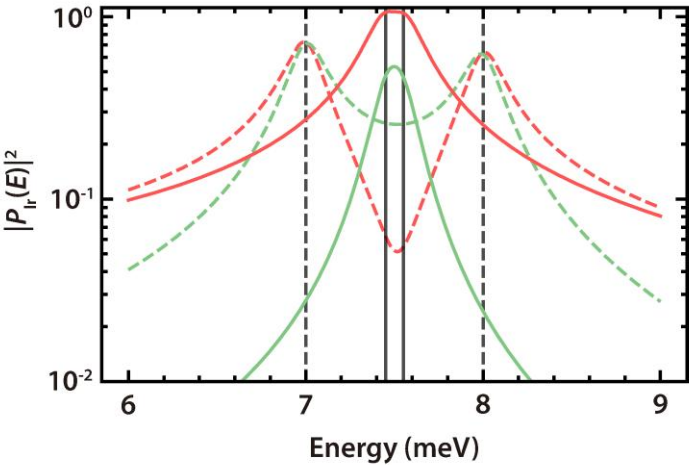

Supplementary Fig. 34 | Model for the interference between two nearly degenerate vibrational modes. Absolute value of the squared propagator $|P_{\mathrm{lr}}(E)|^2$ as a function of energy for constructive interference (green) and destructive interference (red). The dashed lines show the behavior with an energy splitting of the modes of 1 meV. The dashed green line corresponds to enhanced transmission between the modes and the dashed red line to a destructive interference dip. Solid lines show the behavior for nearly degenerate modes at an energy splitting of 0.1 meV. In this case the transmission between the constructively interfering modes is lower than between the destructively interfering ones. A broadening $\eta = 0.1$ meV is used in the plot.

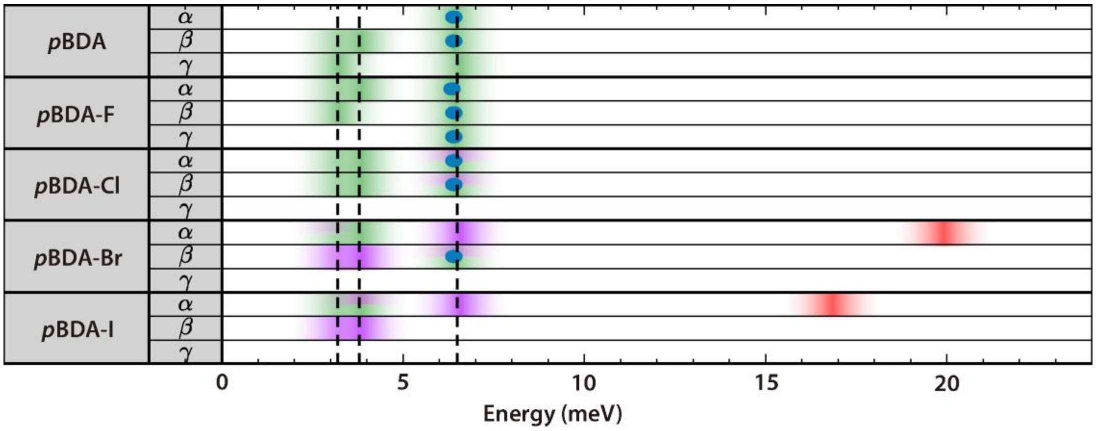

Supplementary Fig. 35 | Summary of interference features for the junction geometries shown in Fig. 5. The interference of vibrational modes is studied for the TEs α, β, and γ at the energies marked in Fig. 5 of the main text. Green boxes indicate constructive interference, while purple boxes indicate lacking interference due to asymmetry of vibrational modes. Split boxes in green and purple signal constructive interferences that are weakened by asymmetry. Blue dots represent constructive interferences that nevertheless lead to a low transmission due to energetic degeneracy of interfering modes. Finally, red boxes show the destructive interferences for *p*BDA-Br and *p*BDA-I MJs.

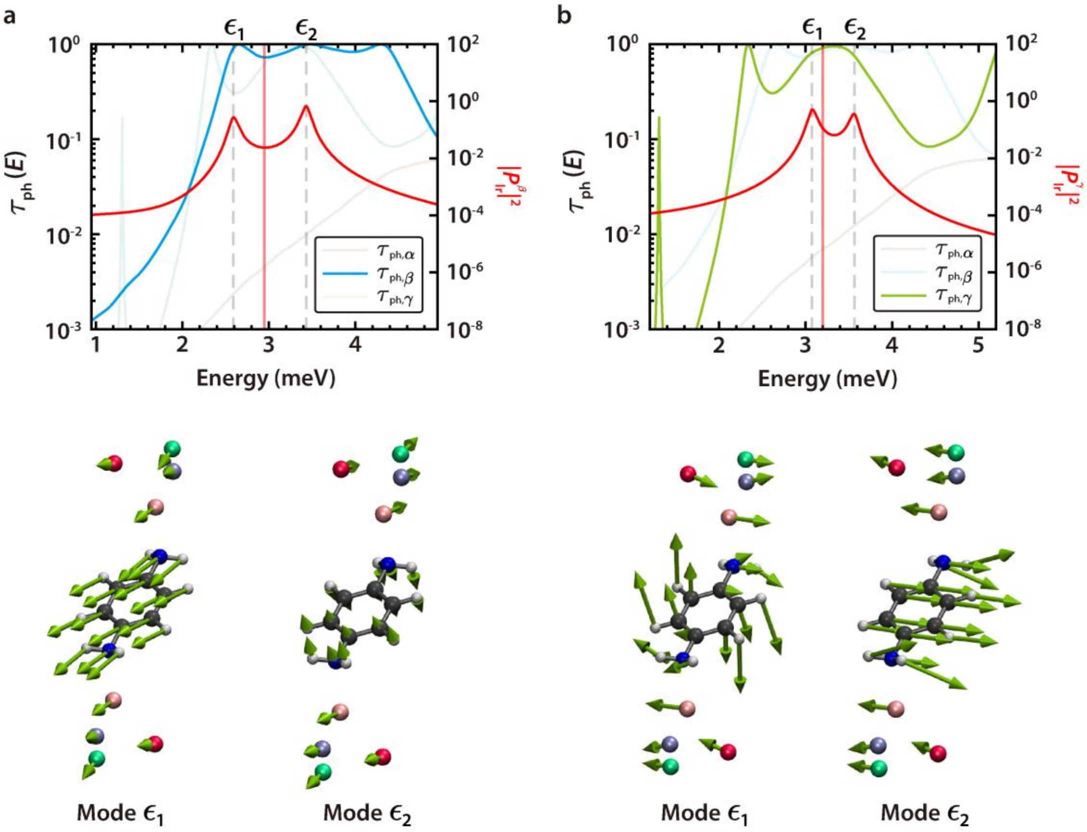

Supplementary Fig. 36 | Analysis of phonon interference for the *p*BDA MJ around 3.2 meV. **a**, Phonon transmission $\tau_{\mathrm{ph},\beta}(E)$ (left axis) and the propagator $|P_{\mathrm{lr}}^{\beta}(E)|^2$ according to Eq. (14) (right axis) as a function of the energy. The red vertical line indicates the energy E_{d}, at which the system was diagonalized. For $|P_{\mathrm{lr}}^{\beta}(E)|^2$ vibrational modes with a threshold $\sigma_{\beta i} > 0.2$ are considered, and a broadening of $\eta = 5 \times 10^{-2}$ meV is used. The eigenmodes 1 and 2 around E_{d} are shown in the lower panel. According to the interference rules, a constructive interference occurs (see atomic displacements of the three colored gold atom pairs at the top and bottom). **b**, Same as (a) but for the TE γ.

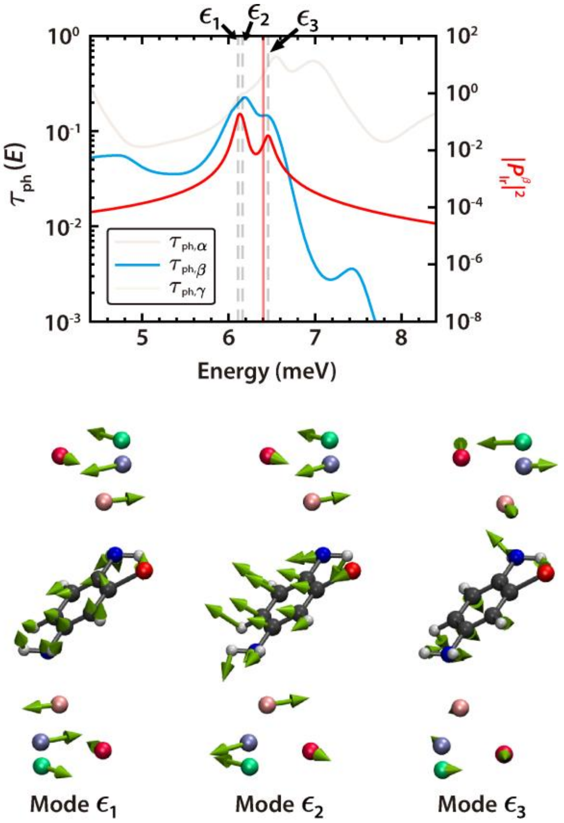

Supplementary Fig. 37 | Analysis of phonon interference for the *p*BDA-Br MJ at 6.4 meV. Same as in Supplementary Fig. 36 but for the *p*BDA-Br MJ.

Table 1. Overview of the thermal conductance results shown in Supplementary Fig. 24b.

Molecular junctions	Average thermal conductance over the displacement ranging from –20 pm to 0 pm (pW/K)	Average thermal conductance over the displacement ranging from –20 pm to –5 pm (pW/K)	Data shown in Fig. 4b obtained from rupture point analysis (pW/K)	Average weight order
*p*BDA	15.82±2.74	17.17±1.52	18.36±2.01	4.58
*p*BDA-F	16.09±1.37	16.68±0.93	17.80±1.11	4.42
*p*BDA-Cl	11.11±1.46	11.65±1.25	12.29±2.49	2.89
*p*BDA-Br	9.97±0.87	10.34±0.65	10.60±1.16	2.06
*p*BDA-I	9.08±0.66	9.37±0.37	9.52±0.68	1.05

Table 2. Overview of the thermal conductance results for the studied molecular junctions.

Molecular junctions	Thermal conductance determined by histogram analysis (pW/K)	Thermal conductance predicted by the DFT calculations (pW/K)
*p*BDA	19.11±0.56	18.34
*p*BDA-F	16.42±0.43	16.27
*p*BDA-Cl	11.96±0.55	14.47
*p*BDA-Br	11.56±1.21	11.15
*p*BDA-I	7.74±1.14	10.05

Supplementary References

1 Wang, S., Zhu, J., Blackwell, R. & Fischer, F. R. Automated tip conditioning for scanning tunneling spectroscopy. *J. Phys. Chem. A* **125**, 1384-1390(2021), doi:10.1021/acs.jpca.0c10731.

2 Berwanger, J., Huber, F., Stilp, F. & Giessibl, F. J. Lateral manipulation of single iron adatoms by means of combined atomic force and scanning tunneling microscopy using CO-terminated tips. *Phys. Rev. B* **98**, 195409(2018), doi:10.1103/PhysRevB.98.195409.

3 Liu, S. *et al.* Resolving the correlation between tip-enhanced resonance Raman scattering and local electronic states with 1 nm resolution. *Nano Lett.* **19**, 5725-5731(2019), doi:10.1021/acs.nanolett.9b02345.

4 Oh, M. *et al.* Evidence for unconventional superconductivity in twisted bilayer graphene. *Nature* **600**, 240-245(2021), doi:10.1038/s41586-021-04121-x.

5 Kim, K. *et al.* Radiative heat transfer in the extreme near field. *Nature* **528**, 387-391(2015), doi:10.1038/nature16070.

6 Yan, S. *et al.* Surface phonon polariton-mediated near-field radiative heat transfer at cryogenic temperatures. *Phys. Rev. Lett.* **131**, 196302(2023), doi:10.1103/PhysRevLett.131.196302.

7 Rytov, S. M., Kravtsov, Y. A. & Tatarskii, V. I. *Principles of statistical radiophysics 2*. 1 edn, (Springer Berlin, Heidelberg, 1988).

8 Derjaguin, B., Abrikosova, I. & Lifshitz, E. Direct measurement of molecular attraction between solids separated by a narrow gap. *Q. Rev., Chem. Soc.* **10**, 295-329(1956), doi:10.1039/QR9561000295.

9 Dechaumphai, E. & Chen, R. Sub-picowatt resolution calorimetry with niobium nitride thin-film thermometer. *Rev. Sci. Instrum.* **85**, 094903(2014), doi:10.1063/1.4895678.

10 Simon, R., Dalrymple, B., Van Vechten, D., Fuller, W. & Wolf, S. Transport measurements in granular niobium nitride cermet films. *Phys. Rev. B* **36**, 1962(1987), doi:10.1103/PhysRevB.36.1962.

11 Ftouni, H. *et al.* Thermal conductivity of silicon nitride membranes is not sensitive to stress. *Phys. Rev. B* **92**, 125439(2015), doi:10.1103/PhysRevB.92.125439.

12 Senturia, S. D. *Microsystem design*. (Springer Science & Business Media, 2005).

13 Xu, B. & Tao, N. Measurement of single-molecule resistance by repeated formation of molecular junctions. *Science* **301**, 1221-1223(2003), doi:10.1126/science.1087481.

14 Lee, W. *et al.* Heat dissipation in atomic-scale junctions. *Nature* **498**, 209-212(2013), doi:10.1038/nature12183.

15 Venkataraman, L., Klare, J. E., Nuckolls, C., Hybertsen, M. S. & Steigerwald, M. L. Dependence of single-molecule junction conductance on molecular conformation. *Nature* **442**, 904-907(2006), doi:10.1038/nature05037.

16 Arroyo, C. R. *et al.* Influence of binding groups on molecular junction formation. *J. Am. Chem. Soc.* **133**, 14313-14319(2011), doi:10.1021/ja201861k.

17 Hong, W. *et al.* Single molecular conductance of tolanes: experimental and theoretical study on the junction evolution dependent on the anchoring group. *J. Am. Chem. Soc.* **134**, 2292-2304(2012), doi:10.1021/ja209844r.

18 Hurtado-Gallego, J. *et al.* Benchmarking break-junction techniques: electric and thermoelectric characterization of naphthalenophanes. *Nanoscale* **16**, 10751-10759(2024), doi:10.1039/D4NR00704B.

19 Yelishala, S. C. *et al.* Phonon interference in single-molecule junctions. *Nat. Mater.* **24**, 1258-1264(2025), doi:10.1038/s41563-025-02195-w.

20 Cui, L. *et al.* Thermal conductance of single-molecule junctions. *Nature* **572**, 628-633(2019), doi:10.1038/s41586-019-1420-z.

21 Mosso, N. *et al.* Thermal transport through single-molecule junctions. *Nano Lett.* **19**, 7614-7622(2019), doi:10.1021/acs.nanolett.9b02089.

22 Gemma, A. *et al.* Full thermoelectric characterization of a single molecule. *Nat. Commun.* **14**, 3868(2023), doi:10.1038/s41467-023-39368-7.

23 Frei, M., Aradhya, S. V., Hybertsen, M. S. & Venkataraman, L. Linker dependent bond rupture force measurements in single-molecule junctions. *J. Am. Chem. Soc.* **134**, 4003-4006(2012), doi:10.1021/ja211590d.

24 van der Poel, S. *et al.* Mechanoelectric sensitivity reveals destructive quantum interference in single-molecule junctions. *Nat. Commun.* **15**, 10097(2024), doi:10.1038/s41467-024-53825-x.

25 Bürkle, M. *et al.* Conduction mechanisms in biphenyl dithiol single-molecule junctions. *Phys. Rev. B* **85**, 075417(2012), doi:10.1103/PhysRevB.85.075417.

26 Blaschke, M. & Pauly, F. Revealing molecule-internal mechanisms that control phonon heat transport through single-molecule junctions by a genetic algorithm. *ACS Nano* **19**, 32093-32107(2025), doi:10.1021/acsnano.5c03690.

27 Paulsson, M. & Brandbyge, M. Transmission eigenchannels from nonequilibrium Green's functions. *Phys. Rev. B* **76**, 115117(2007), doi:10.1103/PhysRevB.76.115117.

28 Hsu, C. *et al.* Mechanical compression in cofacial porphyrin cyclophane pincers. *Chem. Sci.* **13**, 8017-8024(2022), doi:10.1039/d2sc00937d.

29 Klöckner, J. C., Cuevas, J. C. & Pauly, F. Transmission eigenchannels for coherent phonon transport. *Phys. Rev. B* **97**, 155432(2018), doi:10.1103/PhysRevB.97.155432.

30 Brandbyge, M., Sørensen, M. R. & Jacobsen, K. W. Conductance eigenchannels in nanocontacts. *Phys. Rev. B* **56**, 14956(1997), doi:10.1103/PhysRevB.56.14956.

31 Yoshizawa, K. An orbital rule for electron transport in molecules. *Acc. Chem. Res.* **45**, 1612-1621(2012), doi:10.1021/ar300075f.

32 Reznikova, K. *et al.* Substitution pattern controlled quantum interference in [2.2] paracyclophane-based single-molecule junctions. *J. Am. Chem. Soc.* **143**, 13944-13951(2021), doi:10.1021/jacs.1c06966.

33 Stefani, D. *et al.* Large conductance variations in a mechanosensitive single-molecule junction. *Nano Lett.* **18**, 5981-5988(2018), doi:10.1021/acs.nanolett.8b02810.

34 Klöckner, J.-C., Cuevas, J. C. & Pauly, F. Tuning the thermal conductance of molecular junctions with interference effects. *Phys. Rev. B* **96**, 245419(2017), doi:10.1103/PhysRevB.96.245419.

35 Markussen, T. Phonon interference effects in molecular junctions. *J. Chem. Phys.* **139**, 244101(2013), doi:10.1063/1.4849178.

36 Dames, C. & Chen, G. 1ω, 2ω, and 3ω methods for measurements of thermal properties. *Rev. Sci. Instrum.* **76**, 124902(2005), doi:10.1063/1.2130718.

37 Sadat, S., Meyhofer, E. & Reddy, P. High resolution resistive thermometry for micro/nanoscale measurements. *Rev. Sci. Instrum.* **83**, 084902(2012), doi:10.1063/1.4744963.